River Salinity Mapping through Machine Learning and Statistical Modeling using Landsat 8 OLI Imagery

Mohsen Ansari, Anders Knudby, Saeid Homayouni

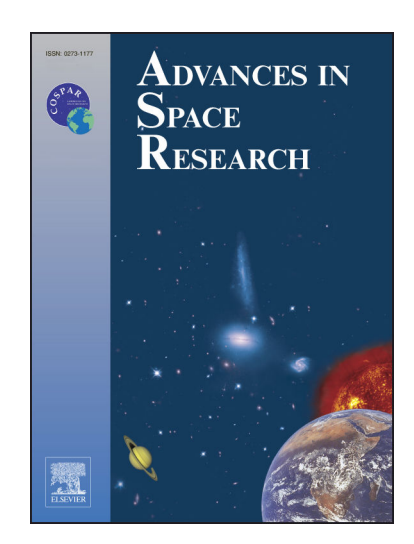
PII: S0273-1177(25)00255-8

DOI: https://doi.org/10.1016/j.asr.2025.03.037

Reference: JASR 18244

To appear in: Advances in Space Research

Received Date: 13 August 2024 Revised Date: 21 February 2025 Accepted Date: 14 March 2025



Please cite this article as: Ansari, M., Knudby, A., Homayouni, S., River Salinity Mapping through Machine Learning and Statistical Modeling using Landsat 8 OLI Imagery, *Advances in Space Research* (2025), doi: https://doi.org/10.1016/j.asr.2025.03.037

This is a PDF file of an article that has undergone enhancements after acceptance, such as the addition of a cover page and metadata, and formatting for readability, but it is not yet the definitive version of record. This version will undergo additional copyediting, typesetting and review before it is published in its final form, but we are providing this version to give early visibility of the article. Please note that, during the production process, errors may be discovered which could affect the content, and all legal disclaimers that apply to the journal pertain.

© 2025 The Author(s). Published by Elsevier B.V. on behalf of COSPAR.

# River Salinity Mapping through Machine Learning and Statistical Modeling using Landsat 8 OLI Imagery

Mohsen Ansari<sup>1\*</sup>, Anders Knudby<sup>1</sup>, Saeid Homayouni<sup>2</sup>

<sup>1</sup>Department of Geography, Environment and Geomatics, University of Ottawa, 75 Laurier Avenue East, Ottawa, Ontario K1N 6N5, Canada

<sup>2</sup>Institut National de la Recherche Scientifique, Centre Eau Terre Environnement, Quebec, Canada

Correspondence details:

Mohsen.Ansari@uottawa.ca

+1 (613) 252 8600

https://orcid.org/0000-0003-1743-7965

Anders Knudby:

aknudby@uottawa.ca

Saeid Homayouni:

saeid.homayouni@inrs.ca

# **Highlights**

- 1. Good statistical performance doesn't ensure uncorrelated residuals, and vice versa.
- 2. GBDT outperformed statistical, kernel, and neural network models in salinity mapping.
- 3. Karun River salinity increases from Gotvand to Ahvaz, due to agriculture & geology.

# River Salinity Mapping through Machine Learning and Statistical Modeling using Landsat 8 OLI Imagery

This study uses Landsat 8 OLI imagery and 102 *in situ* salinity data points to investigate salinity mapping in the Karun River, southwestern Iran. A total of 24 features, including salinity indices and Landsat 8 OLI spectral bands, were

assessed using the Random Forest Feature Importance Score (RFFIS), Sobol' sensitivity analysis, and correlation with salinity to identify the most sensitive features for salinity estimation. These included the Red and Green bands, Salinity index 2-6, Normalized Suspended Material Index (NSMI), and Enhanced Green Ratio Index (EGRI). A total of 24 regression models, including statistical, kernelbased, Neural Network (NN)-based, and Decision Tree (DT)-based models, were evaluated using statistical error metrics and global, as well as local, Moran's I measures of residual spatial autocorrelation. The DT-based models, specifically Gradient Boosted DT (GBDT), outperformed other models, demonstrating low errors, bias, and non-significant residual spatial autocorrelation. Kernel-based models performed better than conventional linear models, while NN models tended to underfit. Residual spatial autocorrelation analysis indicated that models incorporating spatial information reduced residual autocorrelation. Landsat 8 OLI imagery effectively mapped salinity dynamics, revealing increased salinity from Gotvand to Ahvaz city due to agricultural activities and the Gachsaran formation within the reservoir.

Keywords: Water Salinity; Spatial Autocorrelation; Multispectral Imagery; Regression Analysis; Rivers and Estuaries; Machine Learning.

#### 1. Introduction

The salinity of rivers and estuaries is an important water quality parameter (WQP) that influences freshwater supply and human well-being (Cañedo-Argüelles et al., 2016), the suitability of water for irrigation and agriculture (Tessema et al., 2022), the animal species survival (Jualaong et al., 2019), and the growth of aquatic vegetation (Sebilian Wittyngham et al., 2019). Salinity can vary across space and time due to fluctuations in precipitation and runoff in rivers (Sumner and Belaineh, 2005), water circulation (Bowden and Sharaf El Din, 1966), tidal and wind-driven mixing of water masses (Uncles and Stephens, 2011), as well as changes in the volume of freshwater discharge in estuaries (Jiang et al., 2024). Monitoring changes in salinity, therefore, has many practical applications for water management (Dasgupta et al., 2013; Fichez et al., 2017; James et al., 2003). Salinity is the concentration of dissolved salts in a volume of water. The most common salts in water include the cations sodium  $(Na^+)$ , potassium  $(K^+)$ , magnesium  $(Mg^{2+})$ , and calcium  $(Ca^{2+})$ , and the anions chloride  $(Cl^{-})$ , sulfate  $(SO_4^{2-})$ , and bicarbonate ( $HCO_3^-$ ) (El-Swaify, 2000). These ions increase both the salinity and the Electrical Conductivity (EC) of the water, creating a close relationship between salinity and EC that allows salinity to be measured indirectly via EC measurements (Dahaan et al., 2016; El-Swaify, 2000; U.S. Geological Survey, 2019; Wagner et al., 2006), an approach that is typically used instead of direct measurement of salinity (Khorram, 1985; Rusydi, 2018; Wagner et al., 2006). Measurement of EC does not require lab access and can be automated to acquire data at regular intervals, allowing for high-frequency monitoring. However, such tracking is spatially limited to the location at which probes are deployed; effort has therefore also gone into the development of methods to monitor salinity using satellite imagery that can provide less frequent but spatially complete coverage of an area of interest.

The absorption and scattering of light in water, and therefore water colour, is directly influenced by salinity (Röttgers et al., 2014; Zhang et al., 2009; Zhang and Hu, 2021). However, for the salinity variations that are relevant to natural waters, this influence is relatively small compared to that of more optically active water constituents such as chlorophyll-a found in algal particles, coloured dissolved organic matter

(CDOM), and total suspended sediment (TSS) (Mishra et al., 2017). While knowledge of salinity can improve the retrieval of other water quality variables from optical satellite imagery (Werdell et al., 2013) by fine-tuning retrieval algorithms, direct mapping of salinity with inversion algorithms applied to optical satellite data is not currently possible, and direct mapping of salinity from space is limited to microwave instruments that operate at spatial resolutions too coarse to have value for rivers and estuaries (Kerr et al., 2010; Lagerloef et al., 2008). As a result, practical approaches to salinity mapping with optical data have relied on indirect associations between salinity and other water quality parameters that are i) empirically related to salinity and ii) easier to observe with satellite data. For example, many studies report a linear, inverse correlation between salinity and the CDOM absorption coefficient in coastal waters (Blough et al., 1993; Bowers et al., 2004; D'Sa et al., 2000; Hu et al., 2004; Siddorn et al., 2001). Several studies have also observed a relationship between salinity and TSS (Adjovu et al., 2023a, 2023b; Wang and Xu, 2008), noting that they are negatively correlated (Fang et al., 2010; Wang and Xu, 2008). The successful remote sensing of CDOM and TSS and their observed relationships with salinity suggests that salinity can be mapped indirectly using satellite data, either explicitly using TSS and CDOM as proxies or implicitly by using observations at wavelengths where water color is influenced by TSS and CDOM concentrations (Khadim et al., 2017; Nguyen et al., 2018). From a practical perspective, mapping salinity via an explicit relationship with CDOM and/or TSS is demanding because it requires establishing an empirical relationship between salinity and CDOM and/or TSS, which in turn requires suitable data on those variables. The easier approach is to establish an empirical regression relationship directly between salinity and water colour, with the understanding that CDOM and/or TSS are an implicit link between the two.

Three important considerations involve using empirical regression models to monitor salinity in rivers and estuaries: i) *Selecting appropriate satellite data*. Due to the dynamic nature of rivers, salinity varies spatially and temporally. The spatial resolution of the satellite imagery must be sufficient to allow differentiation of salinity between different parts of the area of interest, the sensor should possess spectral bands sensitive to variations in CDOM and/or TSS, and the temporal resolution must be sufficient for specific monitoring requirements. ii) *Feature engineering*. Selecting spectral bands and indices sensitive to variations in CDOM and/or TSS is important to optimize model performance, but including an excessive number of variables can lead to model overfitting (Nguyen et al., 2018). iii) *Model selection and parameter optimization*. A finely tuned and flexible empirical model can help produce accurate salinity estimates because the spectral behavior of CDOM and/or TSS, and the relationships between CDOM/TSS and salinity, can be complex. Especially when *in situ* data are scarce, employing a regression method that prevents underfitting and avoids overfitting is important.

Previous salinity mapping studies have used sensors such as SeaWiFS (D'Sa et al., 2002), Aquarius (Kao et al., 2018), Visible Infrared Imaging Radiometer Suite (VIIRS) (Vandermeulen et al., 2014), and Moderate Resolution Imaging Spectroradiometer (MODIS) - Aqua (DeLuca et al., 2020). However, due to their low spatial resolution, these sensors are unsuitable for most inland waters, especially rivers (Priyadarshini et al., 2023). For salinity mapping of inland waters, previous studies have used the Landsat series of sensors as well as Sentinel-2 MSI and the Advanced Spaceborne Thermal Emission and Reflection Radiometer (ASTER) (**Table 1**). These

sensors have bands suitable for detection of variations in CDOM absorption (Li et al., 2023) and TSS concentration (Adjovu et al., 2023a), and thus indirectly salinity, and they also allow for the generation of spectral indices correlated with salinity (Mejía Ávila et al., 2022) including dedicated salinity indices (Adjovu et al., 2023a, 2022; Ferdous and Rahman, 2020; Maliki et al., 2020), NSMI (Montalvo, 2010), and the normalized difference suspended sediment index (NDSSI) (Hossain et al., 2010). While visible and NIR bands are used in many studies due to their association with absorption peaks of CDOM and/or TSS, the bands and spectral indices used in combination to study salinity differ between studies.

Table 1 lists statistical and Machine Learning (ML) models used to map salinity. These include Linear Regression (LR), Geographically Weighted Regression (GWR), Spatially Weighted Optimization Model (SWOM), Multiple Linear Regression (MLR), DT, Random Forest (RF), Support Vector Regression (SVR), Artificial Neural Network (ANN), Multilayer Perceptron (MLP), Adaptive Neuro-Fuzzy Inference System (ANFIS), Adaptive Boosting (AdaBoost), Light Gradient Boosting Machine (LightGBM), and Extreme Gradient Boosting (XGBoost). LR and MLR are commonly used; however, a key limitation of these models is their inability to generalize across large spatial and temporal scales due to variability in atmospheric and water composition that affects the spectral signatures of WQPs, including CDOM/TSS (Topp et al., 2020). Specifically, riverine WQPs, including CDOM/TSS, vary within and between river catchments (Chang, 2008; Lintern et al., 2018), and a range of relationships exist between spectral signatures, CDOM/TSS, and salinity across different areas. This requires the development of site-specific empirical models and highlights salinity as a non-stationary variable (Xie et al., 2013) due to interactions between land and water, and most importantly saltwater intrusion into estuaries (Jiang et al., 2024). GWR (Xie et al., 2013) SWOM (Khadim et al., 2017) address this challenge by considering spatial dependencies in modeling salinity. While studies have identified geographical location as a crucial variable in some models (Khadim et al., 2017; Nguyen et al., 2018; Urquhart et al., 2012; Xie et al., 2013), such models often lack transferability to different locations.

ML models such as DT (Nguyen et al., 2018), SVR (Ansari and Akhoondzadeh, 2020), and ensemble models like RF (Nguyen et al., 2018), AdaBoost (Borovskaya et al., 2022), LightGBM (Dai et al., 2023), and NN-based models like ANN (Bayati and Danesh-Yazdi, 2021), MLP (Ansari and Akhoondzadeh, 2020), and ANFIS (Bayati and Danesh-Yazdi, 2021) typically outperform the traditional linear and non-linear statistical approaches for modeling salinity (Table 1).

Drawing from Tobler's First Law of Geography (Tobler, 1970), the evaluation of spatial autocorrelation in regression residuals is essential in spatial regression modeling (Feng et al., 2021; Kelly, 2019; Lu et al., 2023; Mabula et al., 2023; Mahboobi et al., 2023; Mainali et al., 2019; Moran, 1950; Peralta et al., 2016; Sotomayor et al., 2023). Firstly, spatial autocorrelation in residuals violates the independence assumption fundamental to regression analysis, leading to biased parameter estimates and incorrect inference. This undermines the reliability of regression results (Higazi et al., 2013). Secondly, detecting spatial patterns in residuals provides insights into the validity of the regression model by revealing whether it adequately captures all spatial dependencies in the data (Kelly, 2019). The presence of spatial autocorrelation in residuals suggests potential unmodeled spatial processes influencing the response variable, pointing to

areas for model refinement (Higazi et al., 2013; Kelly, 2019; Khorram, 1985; Metulini et al., 2018; Xie et al., 2013). However, despite its significance, the investigation of spatial autocorrelation in regression residuals from statistical and ML models remains underexplored, including in salinity modeling studies.

This study collected *in situ* water salinity data from 2013 to 2018 for the Karun River, Iran's longest and highest-discharge river. Agricultural effluents and industrial sewage, often linked to sugarcane development projects (Nahvi et al., 2018), combine with salt dissolution from the Gachsaran Formation within the reservoir behind the Upper Gotvand Dam (Jalali et al., 2019) to contribute to the salinity of the river, generally resulting in increased salinity downstream. Using these data, we modeled the river's salinity with Landsat 8 OLI imagery. Landsat 8 was selected due to its free availability, spatial resolution suitable for our case study, unlike Aquarius, VIIRS, and MODIS, and its full operational status during our field data collection, unlike Sentinel-2, which became operational only after 2015. For this purpose, we leveraged 14 established spectral indices and 24 predictive models from previous studies. Due to the limited number of matchups (102 samples), developing complex novel models, such as those based on NNs, was impractical. Instead, our efforts were directed toward improving input features to achieve better results with this suite of existing models. We comprehensively evaluated the statistical performance metrics associated with each model. Moreover, we investigated the presence of global and local spatial autocorrelation in the residuals of each model. Specifically, we addressed the following questions within the context of Landsat-based salinity modeling in the Karun River: i) Which predictive model performs best regarding statistical metrics and spatial autocorrelation of residuals? ii) What is the relationship between these two aspects of model performance? iii) How do the influences of the Gachsaran Formation versus other factors (e.g., sugar cane projects) contribute to downstream salinity increases?

#### 2. Study area and data

#### 2.1. Study area

The Karun River basin is located in southwestern Iran. It covers an area of ~67,000 km<sup>2</sup> (Shahraki et al., 2023) (Fig. 1). It runs through 16 cities (e.g., Gotvand, Shushtar, Ahvaz, Khorramshahr, and Abadan are shown in green in Fig. 1) and numerous villages and serves various industrial and agricultural purposes, irrigating over 380,000 hectares of the surrounding plains (Shahraki et al., 2023). The Karun River converges with the Arvand (or Shatt al-Arab) River at Khorramshahr before flowing into the Persian Gulf (Fig. 1). Saline discharges originating from arid land, irrigation practices, fish hatcheries, and urban sources (Adib and Javdan, 2015; Nouraki et al., 2021) contribute to elevated salinity levels in the Karun River. Pollution in the Karun River primarily stems from agricultural and industrial waste, often linked to sugar cane projects (Nahvi et al., 2018). Moreover, the construction of the Upper Gotvand Dam (located near Gotvand station in Fig. 1) has created a reservoir that includes the Gachsaran Formation, known for its deposits of gypsum and halite (rock salt) (Bahadori et al., 2011). Since its completion in 2011, the dam has facilitated prolonged contact between the Gachsaran Formation and reservoir water, increasing salinity in the reservoir (Jalali et al., 2019) and hence in the Karun River.

## 2.2. Landsat-8 OLI images

We used 37 Landsat 8 OLI L1 images that are cloud-free at the 8 stations shown in Fig. 1, for the path/row combinations 165/38, 165/39, and 166/38, covering the period from June 2013 to May 2022. With Landsat 8 OLI's 30-meter spatial resolution, and considering the width of the Karun River at the 8 sampling stations (> 30 m) (refer to Fig. 1), the Karun River at these stations can be observed in at least one pixel on a Landsat 8 OLI image. All Landsat 8 OLI images were atmospherically corrected using the Fast Line-of-sight Atmospheric Analysis of Spectral Hypercubes (FLAASH) module (Cooley et al., 2002), and land, defined as pixels with positive Normalized Difference Vegetation Index (NDVI) values, was masked out. Fourteen indices, previously used for modeling soil/water salinity or TSS, were calculated for each pixel. These indices were selected because recent studies have demonstrated that they correlate with soil/water salinity or TSS (Adjovu et al., 2023a, 2022; Aksoy et al., 2022). Although soil salinity differs from water salinity, indices related to soil salinity have been used in previous water salinity studies and have contributed to improving model performance (Adjovu et al., 2022; Ferdous and Rahman, 2020). While other salinity and TSS indices exist, this study focused on those listed by Adjovu et al.(2023a). The selected indices include Salinity indices 1-7, the Normalized Difference Salinity Index (NDSI), NSMI, NDSSI, the Green-Blue Band Ratio (BR), EGRI, the Water-Sediment Ratio Index (WSRI), and NDVI (Table 2).

#### 2.3. In situ salinity data

*In situ* measurements conducted by the Iran Water and Power Resources Development Company (2023) were performed using a WTW - Portable conductivity meter ProfiLine Cond 3310, which is regularly calibrated to ensure accuracy. This device measures EC, which is temperature-dependent (Dahaan et al., 2016; Wagner et al., 2006), and adjusts readings to 25 °C to report *specific conductance* in μS/cm (U.S. Geological Survey, 2019). Salinity was calculated in practical salinity units (psu) from specific conductance using equations from Schemel (2001) (see Eq. S1 and Eq. S2 in supplementary material); we did not correct for pressure because all measurements were conducted near the water surface (Wagner et al., 2006).

In situ salinity data acquired within  $\pm$  two days of a Landsat 8 OLI image (Table 3) were extracted from each station for 102 matchups. It is worth mentioning that although Sentinel-2 has better spatial and spectral resolution compared to Landsat 8 because it was non-operational before 2015 or due to a mismatch with the timing of the field data collection, its matchups would have been limited to only 21, which is insufficient for training machine learning models. As shown in Table 3, matchups were prepared for specific stations on each date, as cloud cover or the absence of field data on the target date limited availability. In 2013 and 2014, 31 and 30 matchups were prepared across various dates and stations, respectively, while in some years, such as 2018 and 2015, the number of matchups decreased to 1 and 9, respectively. Given the extensive length of the Karun River and the five-year timeframe covered by the data, field data collection was economically constrained. Table 4 provides summary statistics for the salinity observed at each of the eight stations. To evaluate the performance of the salinity models, the matchups were randomly split, allocating ~70% (N = 72) for model training and ~30% (N = 30) for model testing (Shahin et al., 2004).

## 3. Methodology

## 3.1. Feature Engineering

This study extracted and analyzed 21 features, including the Coastal Aerosol, visible, NIR, and SWRI spectral bands of Landsat 8 OLI and the 14 indices listed in Table 2. Three feature selection methods were employed to address potential overfitting and reduced interpretability from this large number of features (Bayati and Danesh-Yazdi, 2021; Jiang et al., 2024): RFFIS, Sobol' sensitivity analysis, and confusion matrix.

To calculate the RFFIS, we first trained an RF model (Breiman, 2001) using the training dataset, considering all 21 features. The RF's hyperparameters were fine-tuned using a Genetic Algorithm (GA) from the *PyGAD* Python library (Gad, 2023); implementation details are available in Table S2 in the supplementary material. The RF model constructs multiple regression trees from random training data samples and averages their predictions. Model accuracy is assessed using data not used in building the trees. Feature importance is determined by measuring the increase in prediction error when the values of a feature are permuted, keeping others unchanged (Abdel-Rahman et al., 2013; Menze et al., 2009). RFFIS scores, which range between 0 and 1 and sum to 1 across all features, are then used to identify the most important features for the regression process. Our implementation of RF was carried out in Python using the *Scikit-learn* library.

Sobol' is a global sensitivity analysis method that decomposes variance to quantify each feature's impact on the model output relative to others (Sobol', 1993). The problem formulation is  $Y = f(X) = f(X_1, ..., X_{21})$ , where Y is the model output (i.e., salinity) and  $X = (X_1, ..., X_{21})$  is the feature set (Verrelst and Rivera, 2017). An Ordinary Least Squares (OLS) model with all 21 features and all matchups (N = 102) was used to establish the problem formulation using the *statsmodels* library in Python. In the Sobol' method, the total unconditional variance of Y,V(Y), is decomposed into  $V_i$  $V_{ij}, V_{ijk}, ...V_{1...21}$ , representing contributions from individual factors  $X_i$ , interactions  $X_i$ and  $X_i$ , and higher-order interactions (Homma and Saltelli, 1996; Nossent et al., 2011). Variance is calculated using Monte Carlo integrals and Sobol' quasi-random sampling (Homma and Saltelli, 1996; Nossent et al., 2011), for which 10,000 samples of independent random variables, uniformly distributed within the range of each feature, are generated. The total-order sensitivity indices,  $S_{T_i} = 1 - \frac{V_{\sim i}}{V}$  where  $V_{\sim i}$  is obtained from variation of all parameters, except  $X_i$ , ranging from 0 to 1 and sum to 1 across all features, measure the main effect and interactions of  $X_i$  with other parameters, allowing for the ranking of feature importance (Nossent et al., 2011). Our implementation of Sobol' sensitivity analysis was conducted in Python using the SALib library.

The confusion matrix was generated by calculating the coefficient of determination ( $R^2$ ) values between all 21 features and salinity. The 21 features were then ranked based on their RFFIS,  $S_T$  values, and  $R^2$  values with salinity, from 1 to 21, and the average of these three ranks was computed to determine the final rank. Subsequently, regression models were then trained using the feature with the best average rank, with its hyperparameters optimized by GA, and its  $R^2$  was calculated using the test dataset. This process was repeated, adding one top-ranked feature until all features were included. Finally, each model's features that resulted in the highest  $R^2$  were selected.

## 3.2. Regression Methods

We tested 24 different regression methods for salinity modeling, including statistical, kernel-based, DT-based, and NN-based models. The hyperparameters of all methods, as detailed in Section S3 of the Supplementary Material, were tuned using a GA to ensure optimal performance. All regression models were implemented using Python. We utilized DT, GBDT, Gaussian Process Regression (GPR), Kernel Ridge Regression (KRR), MLP, Partial Least Squares Regression (PLSR), RF, Ridge Linear Regressor (RLR), and SVR from the Scikit-learn library (Buitinck et al., 2013), One-Dimensional Convolutional Neural Network (1D-CNN), ANN, Gated Recurrent Units (GRU), Long Short-Term Memory (LSTM), and Simple Recurrent Neural Network (RNN) from the Keras library (Chollet, 2015), OLS and Generalized Linear Model (GLM) from the statsmodels library (Seabold and Perktold, 2010), Spatial Lag Model (SLM) and Spatial Error Model (SEM) from the sperg library, GWR from the MGWR library (Oshan et al., 2019), Generalized Additive Model (GAM) from the pyGAM library (Servén et al., 2018), Cubist from the Cubist library (Kuhn et al., 2023), LightGBM from LightGBM library (Ke et al., 2017), XGBoost from XGBoost library (Chen and Guestrin, 2016), and ANFIS from Scikit-Fuzzy (Warner et al., 2019).

#### 3.2.1. Statistical Models

OLS assumes that the errors are independent and identically distributed, which may not be the case, especially for spatial data (Xie et al., 2013). To address this limitation, spatial regression methods such as the SLM and SEM (Anselin, 2001) account for spatial autocorrelation by incorporating spatially lagged variables or allowing for spatially correlated error terms (Mainali et al., 2019), respectively. A weight matrix is required to implement the SLM and SEM, reflecting each observation's influence on its neighbors. We calculate the weight matrix using the data's spatial coordinates, with closer observations receiving higher weights. Furthermore, the GWR method (Brunsdon et al., 1998) offers localized modeling capabilities by incorporating spatially varying coefficients based on spatial coordinates. A common challenge in linear modeling is multicollinearity, i.e., highly correlated predictor variables. Models like PLSR (Geladi and Kowalski, 1986) and RLR (Hoerl and Kennard, 1970) address multicollinearity by either performing dimensionality reduction or incorporating a regularization term into the OLS objective function. GAM (Hastie, 1992) and GLM (Gotway and Stroup, 1997) extend the traditional linear modeling framework by accommodating non-linear relationships between predictors and response variables.

## 3.2.2. Kernel-Based Models

A key component of kernel-based models is the *kernel function*, which computes the similarity between pairs of data points in the original input space. We test the Radial Basis Function (RBF), linear, sigmoid, and second-degree polynomial kernels for all kernel-based methods, selecting the one that produces the best results.

GPR (Williams and Rasmussen, 1995) adopts a non-parametric Bayesian approach to model the relationship between input variables and outputs as a distribution over functions. KRR (Vovk, 2013) is a regularized linear regression version, employing kernel functions to map input variables into high-dimensional feature spaces. SVR (Smola and Schölkopf, 2004) builds on support vector machines and seeks a hyperplane that maximizes the margin around the predicted values.

#### 3.2.3. Decision Tree-Based Models

DT-based models recursively split the data into subsets based on features, resulting in a tree structure. Ensemble learning models like RF (Breiman, 2001), XGBoost (Chen and Guestrin, 2016), LightGBM (Ke et al., 2017), and GBDT (Friedman, 2001) try to increase predictive accuracy by using the collective outputs of multiple DTs. Cubist (Quinlan, 1992) builds a series of regression trees to partition the data into smaller subsets similar to the other tree-based models. Within each subset, it fits a linear model, allowing for the capture of local trends.

### 3.2.4. Neural Network-Based Models

Regarding NN-based models, the Adam optimizer was used universally, and the ReLU activation function was applied to the ANN, 1D-CNN, and MLP models, while the linear activation function was used for the GRU, LSTM, and SimpleRNN models, as determined through trial and error. The MLP (Atkinson and Tatnall, 1997) forms the foundation of NNs, consisting of Fully Connected (FC) layers where each neuron in a layer is connected to every neuron in the subsequent layer. The ANN (Paoletti et al., 2019) builds upon the MLP structure but typically incorporates more layers, allowing them to learn increasingly complex data representations. The ANFIS (Jang, 1993) is a fuzzy logic-based ML model that combines fuzzy logic with an NN's structure. The 1D-CNN (Albawi et al., 2017) consists of one-dimensional convolutional layers, enabling them to learn hierarchical features automatically. The RNN (Elman, 1990), LSTM (Hochreiter and Schmidhuber, 1997), and GRU (Cho et al., 2014) models use feedback loops to incorporate previous data as they process new input.

#### 3.3. Model Evaluation

Model performance was assessed using i) evaluation metrics and box plots (range, quartiles, and median) of model estimates and observations and ii) examination of residual spatial autocorrelation globally and locally. The model with the best overall performance in evaluations (i) and (ii) was identified, retrained using all matchups (N = 102), and applied to Landsat 8 OLI images on 19 June 2013; 01 February 2015; 05 September 2018; and 11 May 2022. These dates were selected because there was no cloud cover in the Landsat 8 OLI images of the study area, in situ data were available on 19 June 2013 and 01 February 2015, at salinity sampling stations (Fig. 1) for validation, to allow comparison with salinity maps from previous studies (Ansari and Akhoondzadeh, 2021, 2020), and to evaluate the model across different years and seasons under varying weather conditions. A salinity map was generated in ESRI ArcGIS Pro 3.1.0 for each date. The average salinity within a 1 km buffer around five cities, shown in green in Fig. 1, was calculated. The cities were selected because Gotvand and Abadan are located far upstream and downstream, respectively, and the areas around Shushtar, Ahvaz, and Khorramshahr have sugarcane cultivation that may influence salinity in the Karun River (Moradi-Majd et al., 2022).

#### 3.3.1. Evaluation Metrics

6 statistical metrics were employed as evaluation metrics: linear regression slope, R<sup>2</sup>, Root Mean Square Error (RMSE), Root Mean Squared Logarithmic Error (RMSLE), Median Symmetric Accuracy (ε) (Morley et al., 2018), and Symmetric Signed Percentage Bias (β) (Morley et al., 2018) (Eq. 1-5):

$$R^{2} = \left[ \frac{\sum_{i=1}^{N} (E_{i} - \overline{E}) (O_{i} - \overline{O})}{\sqrt{\sum_{i=1}^{N} (E_{i} - \overline{E})^{2}} \sqrt{\sum_{i=1}^{N} (O_{i} - \overline{O})^{2}}} \right]^{2}$$
(1)

$$RMSE = \sqrt{\frac{1}{N} \sum_{i=1}^{N} (E_i - O_i)^2}$$
 (2)

$$RMSLE = \sqrt{\frac{1}{N} \sum_{i=1}^{N} (\log E_i - \log O_i)^2}$$
 (3)

$$\beta = 100 \times \text{sign}\left[\text{median}\left(\log \frac{E_i}{O_i}\right)\right] \times \left(e^{\left|\text{median}\left(\log \frac{E_i}{O_i}\right)\right|} - 1\right) \tag{4}$$

$$\varepsilon = 100 \times \left( e^{\text{median}\left[\left|\log\left(\frac{E_i}{O_i}\right)\right|\right]} - 1 \right)$$
 (5)

N is the number of observations, and O, E,  $\overline{O}$ , and  $\overline{E}$  are the observations, estimated values, the average, and the average of the estimated values, respectively.

 $R^2$ , a metric ranging from 0 to 1, quantifies the proportion of variance explained by the model, with 1 indicating a perfect fit and values near 0 suggesting no correlation, as frequently used in previous studies in **Table 1**. RMSE measures the average magnitude of errors between predicted and actual values, with lower values indicating better performance. RMSLD, unlike RMSE, considers the logarithmic difference between predicted and actual values, which can be beneficial when dealing with nonnormally distributed errors or outliers as it scales down the impact of outliers (Morley et al., 2018). Additionally,  $\epsilon$  represents a symmetric percentage error, penalizing over- and under-estimation equally. Lower values indicate superior performance, with perfect accuracy assigned a value of 0%. Similarly,  $\beta$ , akin to  $\epsilon$ , represents a percentage bias that maintains symmetry between over- and under-estimation, with values closer to zero indicating better performance. Previous studies (Pahlevan et al., 2022; Smith et al., 2021), have demonstrated that median measures, linear regression slopes, and RMSLD collectively provide a comprehensive framework for evaluating models.

#### 3.3.2. Residual Spatial Autocorrelation

Spatial autocorrelation (Tobler, 1970) occurs when neighboring data points influence each other or are influenced by the same spatially variable process, potentially leading to bias in predictions and a violation of the assumption of independence in standard statistical procedures (Mainali et al., 2019). Autocorrelated model residuals, stemming from this spatial dependence, can lead to overly optimistic conclusions about model performance (Kelly, 2019). Ensuring the validity of regression results, therefore, entails assessing whether residuals are independent and identically distributed (Anselin et al., 2004; Lu et al., 2023; Mabula et al., 2023; Mahboobi et al., 2023; Sotomayor et al., 2023). Moran's I (Moran, 1950) is commonly employed to analyze residual spatial autocorrelation (Mainali et al., 2019). Interpreting Moran's I involves calculating the associated p-value and Z-Score under the null hypothesis of no spatial autocorrelation. A non-significant p-value suggests the absence of significant spatial patterns in the residuals, indicating the model's success in capturing the relationship between the

dependent and spatial variables.

Conversely, a significant p-value indicates significant spatial patterns in the residuals. Positive Z-Scores indicate positive spatial autocorrelation of high and/or low values, while negative Z-Scores indicate negative spatial autocorrelation. Moran's I is calculated as follows:

Moran's I = 
$$\frac{N\sum_{i=1}^{N}\sum_{j=1}^{N}w_{ij}(r_i-\bar{r})(r_j-\bar{r})}{\sum_{i=1}^{N}(r_i-\bar{r})^2(\sum_{i=1}^{N}\sum_{j=1}^{N}w_{ij})}$$
(6)

where r represents the residual values at locations i and j,  $\bar{r}$  denotes the mean of r, and  $w_{ij}$  is a matrix of spatial weights.

Calculating Moran's I requires the weight matrix to account for spatial dependence between sampling points. Each spatial weight represents the relative influence of different spatial units on the candidate spatial unit (Mainali et al., 2019). To calculate Moran's I, we created a weight matrix using the inverse of Haversine distance, giving higher values to closer neighbors. Moran's I values were obtained through 1,000,000 random spatial permutations of the predicted values for each model under the null hypothesis of Complete Spatial Randomness (CSR). The reference distribution for each model, used to evaluate statistical significance, is provided in Fig. S1 in the supplementary material. We also calculated the local Moran's I (Anselin, 1995) to assess whether similar high or low values are located close to each other in geographical space. (Mainali et al., 2019). All spatial analyses were implemented using Python's *PySAL* library (Rey and Anselin, 2010).

#### 4. Results

#### 4.1. Feature Selection

Fig. 2 illustrates the confusion matrix for 21 features and salinity measurements. Table 5 provides the values and ranks of RFFIS,  $S_{Ti}$ , and the correlation with salinity for Landsat 8 OLI spectral bands and indices from Table 2, sorted by mean rank. Details of the OLS model used in Sobol' analysis and the tuned hyperparameters obtained through GA for the RF model are presented in Table S1. According to Table 5, the Red band is identified as the most sensitive feature to salinity. Consequently, all 24 regression models were trained using the Red band, with hyperparameters optimized via GA and  $R^2$  values calculated on the test dataset. This process was repeated iteratively, adding the next top-ranked feature until all features were included. The  $R^2$  values at each step for each model are shown in Fig. 3. Ultimately, the bands yielding the highest  $R^2$  for each model were selected. Table S3 in the supplementary material lists the fine-tuned hyperparameters for each model using the best feature combination.

#### 4.2. Performance Assessment

The RBF kernel achieved better  $R^2$  than other kernels across all models. Hence, we use the RBF kernel for all kernel-based models (see Table S3 in the supplementary material). Fig. 4 shows that the Pearson correlation coefficients for all methods were statistically significant. Cubist, XGBoost, and GBDT had the lowest  $\beta$  values (~0%), with GBDT also having the lowest RMSE (0.10 psu) and  $\epsilon$  (4.62%) and the highest  $R^2$  (0.96). GWR had the slope closest to 1 (1.03), while XGBoost, GBDT, and LightGBM

had the lowest RMSLE (0.11). Fig. 5's box plot reveals that the GBDT, XGBoost, and Cubist models' predictions are closest to the observations based on their median, quartiles, and range.

#### 4.3. Spatial Analysis

Fig. 6 presents the global Moran's I, which equals the average local Moran's I, Z-score, p-value, and the standardized local Moran's I scatter plot for each model. For 11 out of 24 models, the null hypothesis of CSR was rejected (p < 0.05). Among these 11 models, the RF model had the lowest absolute global Moran's I and Z-score, at 0.44 and 2.14, respectively, while the RNN model had the highest absolute global Moran's I and Z-score, at 0.71 and 4.79, respectively. The positive Z-scores for the KRR and RNN models and their standardized local Moran's I scatter plots indicate autocorrelated residuals for these models.

For the remaining 13 models, the null hypothesis of CSR was not rejected, suggesting the absence of significant spatial patterns in the residuals. Among these 13 models, the GWR model had the lowest absolute global Moran's I, at 0.12, and the GPR model had the lowest absolute Z-score, at 0.15. The ANFIS and GAM models had the highest absolute global Moran's I and Z-scores among these models, at 0.36 and 1.8, respectively.

## 4.4. Salinity Maps

Fig. 7 shows salinity maps of the Karun River generated by GBDT. The GBDT was selected because, as discussed in Section 4.2, Cubist, XGBoost, and GBDT generally perform better than other models in terms of  $\beta$ ,  $\epsilon$ , slope,  $R^2$ , error, and box plot metrics (predictions' median, quartiles, and range). XGBoost and GBDT specifically outperform Cubist in  $\epsilon$ , slope,  $R^2$ , error, and predictions' median. Although both XGBoost and GBDT have uncorrelated residuals, the Z-Score and the slope of the OLS fit line between standardized local Moran's I and its spatial lag for GBDT are approximately one-sixth of those for XGBoost [see Fig. 6(n, o)]. We therefore chose GBDT to generate the salinity map. This model, trained on the entire dataset (N=102) and compared to the data from each station, achieved an RMSE of 0.11, ranging from 0.06 at Ahvaz to 0.19 at Abadan (Table 6). Fig. 7(a, b) show the estimated and measured salinity at stations with available data. Table 7 presents the average salinity at 1 km buffers around five cities in the Karun River basin [Fig. 7(c)]. Table 7 shows salinity increases from Gotvand to Ahvaz city on all four dates.

## 5. Discussion

#### 5.1. Key Indices and Band Combinations for Salinity Mapping

As shown in Table 5, three different feature selection approaches ranked the features differently: Sobol' by variance analysis, RFFIS by permutation, and the confusion matrix by correlation with salinity. For example, NSMI is ranked first in both RFFIS and correlation but  $10^{th}$  in terms of  $S_T$ . Similarly, Salinity Index 5 is ranked  $15^{th}$  and  $10^{th}$  for  $S_T$  and correlation with salinity, respectively, but  $2^{nd}$  in RFFIS. Therefore, sorting the features by their mean rank allows for identifying those most sensitive to salinity, considering the different criteria used by the three feature selection methods. As shown in Fig. 3, all models ultimately used features ranked 1 to 9, indicating that these are the

most sensitive features. Among these nine features, NSMI and EGRI have relatively low correlation with the others, as illustrated in Fig. 2.

Most of the indices in Table 2 rely on visible spectral bands, which respond to variations in CDOM absorption and TSS (Mishra et al., 2017). As CDOM moves through an estuary, its photochemical reactivity and optical properties may change based on salinity due to changes in CDOM conformation, iron CDOM photochemistry, or both (Minor et al., 2006). This might explain why the Red band was the most sensitive feature in our study (Table 5) and previous studies (Khorram, 1985; Mushtaq and Nee Lala, 2017). The NSMI index, also selected, estimates TSS (Hossain et al., 2010; Malahlela, 2019), which is inversely correlated with salinity. Our study also used salinity indices 2-6, which highly correlate with each other (Fig. 2), consistent with previous studies (Adjovu et al., 2022; Chatterjee and Bhadra, 2023; Liu et al., 2023), indicating that the NIR band is valuable for salinity mapping, especially in turbid waters, where longer wavelengths are more sensitive and saturate at higher TSS concentrations than shorter wavelengths (Mishra et al., 2017).

Previous studies of the Karun River using the same dataset (Ansari and Akhoondzadeh, 2021, 2020) used the Coastal Aerosol, Blue, and Green bands, but this study selected the EGRI index, which combines these bands. Therefore, it is recommended that future research consider both spectral bands and indices followed by feature selection to determine the best combination, as band combinations (i.e., indices) might have higher feature importance than individual bands.

# 5.2. Performance Evaluation across Regression Models: Accuracy and Error Analysis

Regarding the statistical models, GAM showed good performance with higher  $R^2$  and nearly half the RMSE and RMSLD compared to other statistical models. However, the linear regression fit for predicted versus observed salinity relationships showed a closer-to-unity slope for GWR (1.03), indicating superior fit across the entire range [Fig. 4 (c)] compared to other models. Scatterplots in Fig. 4 show a trend where, except for GAM, SLM, and GWR, other statistical models tended to overestimate salinity for values below one psu and underestimate it for values above 1.5 psu, consistent with their respective  $\beta$  values ranging from -6.87% (PLSR) to -4.33% (RLR).

While the performance of all kernel-based models was similar, SVR slightly outperformed the others across all six metrics. All three kernel-based models outperformed 5 out of 8 statistical models implemented in the study (except for GAM, GWR, and SLM). Notably, despite KRR being a linear model leveraging kernel methods, it improved R<sup>2</sup> by ~50% on average over statistical models (except for GAM and GWR), demonstrating the effectiveness of kernel methods in practice.

The NN-based models exhibited weaker performance than other regression model types, characterized by large negative  $\beta$  values (on average -3.72%), indicating underfitting likely due to the scarce training dataset (N = 72). Reported slopes (on average 0.42) indicate poor performance of these models, particularly evident at the tails of data distributions (salinity < 0.5 psu and salinity > 1.5 psu). Due to the limited training dataset, which was insufficient for optimal performance of NN-based models, certain outcomes deviated from theoretical expectations. For instance, while LSTM is designed to address the gradient anomaly issue in RNN effectively and is theoretically

expected to outperform RNN, it performed slightly worse than RNN. Other models (e.g., DT-based models) were also anticipated to yield better results, as the available data was not ideal for effective NN training. It is worth noting that NN-based models like ANN performed better in a previous study (Dai et al., 2023), where a larger dataset of 2,000 matchups was available; their performance relative to other model types might also be improved for the Karun River with a larger dataset. Among the NN-based models implemented, MLP outperformed the others across all six metrics.

Overall, DT-based models outperformed the other model classes. XGBoost and GBDT performed similarly, with negligible  $\beta$ , low  $\epsilon$  (< 5.1%), slope values close to unity (0.9), R² values > 0.93, and low error values (RMSE < 0.13 psu, and RMSLD = 0.11). Scatterplots of XGBoost and GBDT in Fig. 4(n, o) indicate a good fit across the entire value range. LightGBM also had good accuracy with low error, though its median and range of predictions differed more from the observations than XGBoost and GBDT (Fig. 5). Interestingly, although XGBoost and GBDT improved R² and nearly halved RMSE compared to Cubist, Cubist had the lowest possible bias ( $\beta$  = 0.00%), with its boxplot range and quartiles closely matching the observation boxplot (Fig. 5). Overall, XGBoost, GBDT, and Cubist outperformed other regression models in terms of statistical metrics.

## 5.3. Residual Spatial Autocorrelation Analysis

As shown in Fig. 6, the analysis of residual spatial autocorrelation offers additional insight into the performance of different regression models. Among the statistical models, GWR and SLM showed non-significant residual spatial autocorrelation, which was expected because these two models incorporate spatial location in modeling. Interestingly, SLM has a lower absolute Z-Score value (-0.8) than GAM (1.8) [Fig. 6 (a, g)] but performs worse than GAM in terms of all statistical metrics evaluated [Fig. 4 (a, g) and Fig. 5]. For kernel-based models, despite KRR having better accuracy and error performance than GPR [Fig. 4 (i, j)], its Z-score was nearly ten times higher than that of GPR [Fig. 6 (i, j)]. Regarding NN-based models, the ANFIS Z-Score is about half that of the CNN Z-Score, but CNN has better R<sup>2</sup> and RMSE [Fig. 4 (r, t)].

The performance of LightGBM is notable, as shown in Fig. 4 (p), with good results in terms of accuracy ( $R^2 = 0.94$  and  $\epsilon = 8.13\%$ ), bias ( $\beta = 0.7\%$ ), and error (RMSE and RMSLD < 0.13). However, its residuals are significantly autocorrelated (Z-Score = 2.25) [Fig. 6 (p)]. Conversely, GPR shows the lowest non-significant absolute Z-Score value (0.15) [Fig. 6 (i)] despite not having the best accuracy and error performance compared to all models [Fig. 4 (i)]. XGBoost and GBDT perform similarly in accuracy and error [Fig. 4 (n, o)]. Although both have uncorrelated residuals [Fig. 6 (n, o)], GBDT's Z-Score is near one-sixth of XGBoost's Z-Score, and there is no sign of residual spatial autocorrelation in GBDT's local Moran's I scatterplot.

In summary, different models have different performances, and a model's good performance in terms of  $R^2$ , slope,  $\beta$ ,  $\epsilon$ , RMSE, RMSLD, and box plot does not guarantee uncorrelated residuals and vice versa (e.g., GPR and LightGBM in this study). Therefore, checking statistical performance metrics and residual autocorrelation is essential when assessing models. Regression results should be cautiously approached if residual spatial autocorrelation statistics are not reported (Kelly, 2019), as failing to account for this autocorrelation in the evaluation can lead to overestimating the model's performance (Gray et al., 2024). If the residuals are autocorrelated, good statistical

performance can be misleading because the model might capture the autocorrelation structure rather than the true relationship between the independent and dependent variables. This can alter the gradient of the parameter of interest (in this case, salinity) globally and locally.

#### 5.4. Salinity Map Validation

The salinity maps in Fig. 7 (b, c) are consistent with previous observations, where Ansari and Akhoondzadeh (2021, 2020) demonstrated that the Karun River became increasingly saline from upstream to downstream on 01 February 2015, and 05 September 2018.

Considering that there is no sampling station in the reservoir and only one sampling station after the confluence with the Arvand River (i.e., Abadan), the lack of local validation renders the regression model output more uncertain in these areas. As shown in Table 6, the RMSE for Abadan (0.19 psu) is the highest of any station, illustrating the increased uncertainty in this area. However, from Gotvand to Ahvaz, given the six sampling stations and the good performance of GBDT in terms of statistical metrics and residual autocorrelation analysis, the salinity maps can be considered more reliable (RMSE < 0.13 psu).

Based on Fig. 7, and especially Fig. 7 (d), a general increase in salinity is observed from the upstream end of the reservoir to the dam, suggesting that water becomes saltier due to prolonged contact with the Gachsaran formation, which is consistent with a previous study (Jalali et al., 2019). However, the Gachsaran formation is unlikely to be the sole cause of salinity in the Karun River because of the observed increase in salinity from Gotvand to Ahvaz city. According to Table 7, salinity increased on average by more than 34% from Gotvand to Ahvaz city across four different dates. The salinity increase from the reservoir to Gotvand across these dates is notably smaller than that observed from Gotvand to Ahvaz city, indicating that additional factors influence salinity levels in the river at Ahvaz. In this regard, the widespread cultivation of sugarcane in Shushtar and Ahvaz city (Moradi-Majd et al., 2022), which produces agricultural waste, may also contribute to the increased salinity observed from Gotvand to Ahvaz. Specifically, sugarcane production in the Karun basin exacerbates salinity due to several interconnected factors (Ghadiri, 2016): the land selected for sugarcane cultivation is characterized by saline and shallow groundwater, which, when used for irrigation, introduces salt into the soil and eventually into the river. To manage these saline lands, a drainage system is employed, involving the leaching of salt from the soil by applying large volumes of water, which then drains into a collection system. This drainage water, containing both irrigation water and naturally saline groundwater, is subsequently pumped back into the Karun River, further increasing its salinity.

Regarding Khorramshahr city, as shown in Fig. 7 and Table 7, the salinity on four different dates is inconsistent compared to Ahvaz city. The average salinity in Khorramshahr was relatively similar to Ahvaz on 19 June 2013, was lower by over 56% on 01 February 2015, and 05 September 2018, and was higher on 11 May 2022. This variability could be due to the model's lack of calibration at downstream points or the influence of water inflow from the Arvand River (see Fig. 1) (Maliki et al., 2020) near Khorramshahr, affecting downstream WQP in the Karun River.

#### 6. Conclusion

ML models, especially DT-based models like GBDT, outperformed traditional statistical models for mapping salinity in the Karun River using Landsat 8 OLI imagery. The Red band, Green band, NSMI, EGRI, and Salinity indices 2-6 were the most important spectral features for salinity prediction.

Results show that models with good statistical performance cannot guarantee uncorrelated residuals and vice versa. Regression results should be cautiously approached if spatial autocorrelation statistics are not reported. Models like GWR and SLM, which incorporate spatial information, effectively addressed residual autocorrelation.

Landsat 8 OLI imagery successfully mapped salinity dynamics in the Karun River. Salinity increased from Gotvand to Ahvaz city, likely due to agricultural and industrial activities such as sugarcane plantations. Future research should incorporate additional datasets to provide a more detailed examination of the influence of various natural (e.g., geology) and anthropogenic (e.g., land use) factors affecting salinity along the Karun River.

#### Acknowledgments

The authors acknowledge the Iran Water and Power Recourses Development Company for providing the *in situ* water salinity data and the US Geological Survey (USGS) for providing Landsat-8 OLI images.

## **Declaration of Competing Interest**

The authors declare that they have no known competing financial interests or personal relationships that could have appeared to influence the work reported in this paper.

#### Declaration of generative AI and AI-assisted technologies in the writing process

During the preparation of this work the author(s) used OpenAI's ChatGPT for English grammar corrections. After using this tool, the author(s) reviewed and edited the content as needed and take(s) full responsibility for the content of the publication.

#### References

- Abdelmalik, K.W., 2018. Role of statistical remote sensing for Inland water quality parameters prediction. Egypt. J. Remote Sens. Space Sci. 21, 193–200. https://doi.org/10.1016/j.ejrs.2016.12.002
- Abdel-Rahman, E.M., Ahmed, F.B., Ismail, R., 2013. Random forest regression and spectral band selection for estimating sugarcane leaf nitrogen concentration using EO-1 Hyperion hyperspectral data. Int. J. Remote Sens. 34, 712–728. https://doi.org/10.1080/01431161.2012.713142

- Adib, A., Javdan, F., 2015. Interactive approach for determination of salinity concentration in tidal rivers (Case study: The Karun River in Iran). Ain Shams Eng. J. 6, 785–793. https://doi.org/10.1016/j.asej.2015.02.005
- Adjovu, G.E., Stephen, H., Ahmad, S., 2022. Monitoring of Total Dissolved Solids Using Remote Sensing Band Reflectance and Salinity Indices: A Case Study of the Imperial County Section, AZ-CA, of the Colorado River, in: World Environmental and Water Resources Congress 2022. American Society of Civil Engineers, pp. 1132–1145. https://doi.org/10.1061/9780784484258.106
- Adjovu, G.E., Stephen, H., James, D., Ahmad, S., 2023a. Measurement of Total Dissolved Solids and Total Suspended Solids in Water Systems: A Review of the Issues, Conventional, and Remote Sensing Techniques. Remote Sens. 15, 3534. https://doi.org/10.3390/rs15143534
- Adjovu, G.E., Stephen, H., James, D., Ahmad, S., 2023b. Overview of the Application of Remote Sensing in Effective Monitoring of Water Quality Parameters. Remote Sens. 15, 1938. https://doi.org/10.3390/rs15071938
- Aksoy, S., Yildirim, A., Gorji, T., Hamzehpour, N., Tanik, A., Sertel, E., 2022.

  Assessing the performance of machine learning algorithms for soil salinity mapping in Google Earth Engine platform using Sentinel-2A and Landsat-8 OLI data. Adv. Space Res. 69, 1072–1086. https://doi.org/10.1016/j.asr.2021.10.024
- Albawi, S., Mohammed, T.A., Al-Zawi, S., 2017. Understanding of a convolutional neural network, in: 2017 International Conference on Engineering and Technology (ICET). Presented at the 2017 International Conference on Engineering and Technology (ICET), pp. 1–6. https://doi.org/10.1109/ICEngTechnol.2017.8308186
- Ansari, M., Akhoondzadeh, M., 2021. Generation of Karun River Water Salinity Map from Landsat-8 Satellite Images using Support Vector Regression, Multilayer Perceptron and Genetic Algorithm. J. Environ. Stud. 46, 581–600. https://doi.org/10.22059/jes.2021.317955.1008130
- Ansari, M., Akhoondzadeh, M., 2020. Mapping water salinity using Landsat-8 OLI satellite images (Case study: Karun basin located in Iran). Adv. Space Res. 65, 1490–1502. https://doi.org/10.1016/j.asr.2019.12.007
- Ansari, M., Akhoondzadeh, M., 2019. Water Salinity Mapping of Karun Basin Located In Iran Using the SVR Method, in: The International Archives of the Photogrammetry, Remote Sensing and Spatial Information Sciences. pp. 97–101. https://doi.org/10.5194/isprs-archives-XLII-4-W18-97-2019
- Anselin, L., 2001. Rao's score test in spatial econometrics. J. Stat. Plan. Inference, Rao's Score Test 97, 113–139. https://doi.org/10.1016/S0378-3758(00)00349-9
- Anselin, L., 1995. Local Indicators of Spatial Association—LISA. Geogr. Anal. 27, 93–115. https://doi.org/10.1111/j.1538-4632.1995.tb00338.x

- Anselin, L., Bongiovanni, R., Lowenberg-DeBoer, J., 2004. A Spatial Econometric Approach to the Economics of Site-Specific Nitrogen Management in Corn Production. Am. J. Agric. Econ. 86, 675–687. https://doi.org/10.1111/j.0002-9092.2004.00610.x
- Atkinson, P.M., Tatnall, A.R.L., 1997. Introduction Neural networks in remote sensing. Int. J. Remote Sens. 18, 699–709. https://doi.org/10.1080/014311697218700
- Bahadori, A., Carranza, E.J.M., Soleimani, B., 2011. Geochemical analysis of evaporite sedimentation in the Gachsaran Formation, Zeloi oil field, southwest Iran. J. Geochem. Explor., Geochemistry for Geological-Environmental Studies 111, 97–112. https://doi.org/10.1016/j.gexplo.2011.02.007
- Bayati, M., Danesh-Yazdi, M., 2021. Mapping the spatiotemporal variability of salinity in the hypersaline Lake Urmia using Sentinel-2 and Landsat-8 imagery. J. Hydrol. 595, 126032. https://doi.org/10.1016/j.jhydrol.2021.126032
- Blough, N.V., Zafiriou, O.C., Bonilla, J., 1993. Optical absorption spectra of waters from the Orinoco River outflow: Terrestrial input of colored organic matter to the Caribbean. J. Geophys. Res. Oceans 98, 2271–2278. https://doi.org/10.1029/92JC02763
- Borovskaya, R., Krivoguz, D., Chernyi, S., Kozhurin, E., Khorosheltseva, V., Zinchenko, E., 2022. Surface Water Salinity Evaluation and Identification for Using Remote Sensing Data and Machine Learning Approach. J. Mar. Sci. Eng. 10, 257. https://doi.org/10.3390/jmse10020257
- Bouaziz, M., Matschullat, J., Gloaguen, R., 2011. Improved remote sensing detection of soil salinity from a semi-arid climate in Northeast Brazil. Comptes Rendus Géoscience 343, 795–803. https://doi.org/10.1016/j.crte.2011.09.003
- Bowden, K.F., Sharaf El Din, S.H., 1966. Circulation, Salinity and River Discharge in the Mersey Estuary. Geophys. J. Int. 10, 383–399. https://doi.org/10.1111/j.1365-246X.1966.tb03066.x
- Bowers, D.G., Evans, D., Thomas, D.N., Ellis, K., Williams, P.J. le B., 2004. Interpreting the colour of an estuary. Estuar. Coast. Shelf Sci. 59, 13–20. https://doi.org/10.1016/j.ecss.2003.06.001
- Breiman, L., 2001. Random Forests. Mach. Learn. 45, 5–32. https://doi.org/10.1023/A:1010933404324
- Brunsdon, C., Fotheringham, S., Charlton, M., 1998. Geographically Weighted Regression. J. R. Stat. Soc. Ser. Stat. 47, 431–443. https://doi.org/10.1111/1467-9884.00145
- Buitinck, L., Louppe, G., Blondel, M., Pedregosa, F., Mueller, A., Grisel, O., Niculae, V., Prettenhofer, P., Gramfort, A., Grobler, J., Layton, R., Vanderplas, J., Joly, A., Holt, B., Varoquaux, G., 2013. API design for machine learning software: experiences from the scikit-learn project. https://doi.org/10.48550/arXiv.1309.0238

- Cañedo-Argüelles, M., Hawkins, C.P., Kefford, B.J., Schäfer, R.B., Dyack, B.J., Brucet, S., Buchwalter, D., Dunlop, J., Frör, O., Lazorchak, J., Coring, E., Fernandez, H.R., Goodfellow, W., Achem, A.L.G., Hatfield-Dodds, S., Karimov, B.K., Mensah, P., Olson, J.R., Piscart, C., Prat, N., Ponsá, S., Schulz, C.-J., Timpano, A.J., 2016. Saving freshwater from salts. Science 351, 914–916. https://doi.org/10.1126/science.aad3488
- Chang, H., 2008. Spatial analysis of water quality trends in the Han River basin, South Korea. Water Res. 42, 3285–3304. https://doi.org/10.1016/j.watres.2008.04.006
- Chatterjee, S., Bhadra, T., 2023. Assessing the Water Quality of Indian Sundarban Estuaries using Remote Sensing Techniques, in: IOP Conference Series: Earth and Environmental Science. IOP Publishing, p. 012006. https://doi.org/10.1088/1755-1315/1164/1/012006
- Chen, T., Guestrin, C., 2016. XGBoost: A Scalable Tree Boosting System, in:
  Proceedings of the 22nd ACM SIGKDD International Conference on
  Knowledge Discovery and Data Mining, KDD '16. Association for Computing
  Machinery, New York, NY, USA, pp. 785–794.
  https://doi.org/10.1145/2939672.2939785
- Cho, K., van Merrienboer, B., Gulcehre, C., Bahdanau, D., Bougares, F., Schwenk, H., Bengio, Y., 2014. Learning Phrase Representations using RNN Encoder-Decoder for Statistical Machine Translation. https://doi.org/10.48550/arXiv.1406.1078
- Chollet, F., 2015. keras.
- Cooley, T., Anderson, G.P., Felde, G.W., Hoke, M.L., Ratkowski, A.J., Chetwynd, J.H., Gardner, J.A., Adler-Golden, S.M., Matthew, M.W., Berk, A., Bernstein, L.S., Acharya, P.K., Miller, D., Lewis, P., 2002. FLAASH, a MODTRAN4-based atmospheric correction algorithm, its application and validation, in: IEEE International Geoscience and Remote Sensing Symposium. Presented at the IEEE International Geoscience and Remote Sensing Symposium, pp. 1414–1418 vol.3. https://doi.org/10.1109/IGARSS.2002.1026134
- Dahaan, S.A.M.A., Al-Ansari, N., Knutsson, S., 2016. Influence of Groundwater Hypothetical Salts on Electrical Conductivity Total Dissolved Solids. Engineering 8, 823–830. https://doi.org/10.4236/eng.2016.811074
- Dai, J., Liu, T., Zhao, Y., Tian, S., Ye, C., Nie, Z., 2023. Remote sensing inversion of the Zabuye Salt Lake in Tibet, China using LightGBM algorithm. Front. Earth Sci. 10. https://doi.org/10.3389/feart.2022.1022280
- Dasgupta, S., Akhter Kamal, F., Huque Khan, Z., Choudhury, S., Nishat, A., 2013. River Salinity and Climate Change: Evidence from Coastal Bangladesh, in: World Scientific Reference on Asia and the World Economy. World Scientific, pp. 205–242. https://doi.org/10.1142/9789814578622\_0031
- DeLuca, N.M., Zaitchik, B.F., Guikema, S.D., Jacobs, J.M., Davis, B.J.K., Curriero, F.C., 2020. Evaluation of remotely sensed prediction and forecast models for

- *Vibrio parahaemolyticus* in the Chesapeake Bay. Remote Sens. Environ. 250, 112016. https://doi.org/10.1016/j.rse.2020.112016
- Douaoui, A.E.K., Nicolas, H., Walter, C., 2006. Detecting salinity hazards within a semiarid context by means of combining soil and remote-sensing data. Geoderma 134, 217–230. https://doi.org/10.1016/j.geoderma.2005.10.009
- D'Sa, E.J., Hu, C., Muller-Karger, F.E., Carder, K.L., 2002. Estimation of colored dissolved organic matter and salinity fields in case 2 waters using SeaWiFS: Examples from Florida Bay and Florida Shelf. J. Earth Syst. Sci. 111, 197–207. https://doi.org/10.1007/BF02701966
- D'Sa, E.J., Zaitzeff, J.B., Steward, R.G., 2000. Monitoring water quality in Florida Bay with remotely sensed salinity and in situ bio-optical observations. Int. J. Remote Sens. 21, 811–816. https://doi.org/10.1080/014311600210605
- Elman, J.L., 1990. Finding Structure in Time. Cogn. Sci. 14, 179–211. https://doi.org/10.1207/s15516709cog1402\_1
- El-Swaify, S.A., 2000. Soil and Water Salinity, in: Plant Nutrient Management in Hawaii's Soils: Approaches for Tropical and Subtropical Agriculture, Chapter 17. University of Hawaii, pp. 151–158.
- Fang, L., Chen, S., Wang, H., Qian, J., Zhang, L., 2010. Detecting marine intrusion into rivers using EO-1 ALI satellite imagery: Modaomen Waterway, Pearl River Estuary, China. Int. J. Remote Sens. 31, 4125–4146. https://doi.org/10.1080/01431160903229218
- Feng, L., Wang, Y., Zhang, Z., Du, Q., 2021. Geographically and temporally weighted neural network for winter wheat yield prediction. Remote Sens. Environ. 262, 112514. https://doi.org/10.1016/j.rse.2021.112514
- Ferdous, J., Rahman, M.T.U., 2020. Developing an empirical model from Landsat data series for monitoring water salinity in coastal Bangladesh. J. Environ. Manage. 255, 109861. https://doi.org/10.1016/j.jenvman.2019.109861
- Ferdous, J., Rahman, M.T.U., Ghosh, S.K., 2019. Detection of Total Dissolved Solids from Landsat 8 OLI Image in Coastal Bangladesh, in: The International Conference on Climate Change, 1. pp. 35–44. https://doi.org/10.17501/2513258X.2019.3103
- Fichez, R., Archundia, D., Grenz, C., Douillet, P., Gutiérrez Mendieta, F., Origel Moreno, M., Denis, L., Contreras Ruiz Esparza, A., Zavala-Hidalgo, J., 2017. Global climate change and local watershed management as potential drivers of salinity variation in a tropical coastal lagoon (Laguna de Terminos, Mexico). Aquat. Sci. 79, 219–230. https://doi.org/10.1007/s00027-016-0492-1
- Friedman, J.H., 2001. Greedy Function Approximation: A Gradient Boosting Machine. Ann. Stat. 29, 1189–1232.
- Gad, A.F., 2023. PyGAD: an intuitive genetic algorithm Python library. Multimed. Tools Appl. https://doi.org/10.1007/s11042-023-17167-y

- Geladi, P., Kowalski, B.R., 1986. Partial least-squares regression: a tutorial. Anal. Chim. Acta 185, 1–17. https://doi.org/10.1016/0003-2670(86)80028-9
- Ghadiri, H., 2016. Salinization of Karun River in Iran by shallow groundwater and seawater encroachment. Adv. Hydro-Sci. -Eng. 4, 1–9.
- Gotway, C.A., Stroup, W.W., 1997. A Generalized Linear Model Approach to Spatial Data Analysis and Prediction. J. Agric. Biol. Environ. Stat. 2, 157–178. https://doi.org/10.2307/1400401
- Gray, P.C., Boss, E., Prochaska, J.X., Kerner, H., Demeaux, C.B., Lehahn, Y., 2024. The Promise and Pitfalls of Machine Learning in Ocean Remote Sensing.
- Hastie, T.J., 1992. Generalized Additive Models, in: Statistical Models in S. Routledge.
- Higazi, S.F., Abdel-Hady, D.H., Al-Oulfi, S.A., 2013. Application of Spatial Regression Models to Income Poverty Ratios in Middle Delta Contiguous Counties in Egypt. Pak. J. Stat. Oper. Res. 9, 93. https://doi.org/10.18187/pjsor.v9i1.272
- Hochreiter, S., Schmidhuber, J., 1997. Long Short-Term Memory. Neural Comput. 9, 1735–1780. https://doi.org/10.1162/neco.1997.9.8.1735
- Hoerl, A.E., Kennard, R.W., 1970. Ridge Regression: Biased Estimation for Nonorthogonal Problems. Technometrics 12, 55–67. https://doi.org/10.1080/00401706.1970.10488634
- Homma, T., Saltelli, A., 1996. Importance measures in global sensitivity analysis of non-linear models. Reliab. Eng. Syst. Saf. 52, 1–17. https://doi.org/10.1016/0951-8320(96)00002-6
- Hossain, A.K.M.A., Chao, X., Jia, Y., 2010. Development of Remote Sensing Based Index for Estimating/Mapping Suspended Sediment Concentration in River and Lake Environments, in: Proceedings of 8th International Symposium on ECOHYDRAULICS (ISE 2010). pp. 578–585.
- Hu, C., Chen, Z., Clayton, T.D., Swarzenski, P., Brock, J.C., Muller–Karger, F.E., 2004. Assessment of estuarine water-quality indicators using MODIS medium-resolution bands: Initial results from Tampa Bay, FL. Remote Sens. Environ. 93, 423–441. https://doi.org/10.1016/j.rse.2004.08.007
- Iran Water and Power Resources Development Company [WWW Document], 2023. URL https://iwpco.ir/?l=EN (accessed 11.23.23).
- Jalali, L., Zarei, M., Gutiérrez, F., 2019. Salinization of reservoirs in regions with exposed evaporites. The unique case of Upper Gotvand Dam, Iran. Water Res. 157, 587–599. https://doi.org/10.1016/j.watres.2019.04.015
- James, K.R., Cant, B., Ryan, T., 2003. Responses of freshwater biota to rising salinity levels and implications for saline water management: a review. Aust. J. Bot. 51, 703–713. https://doi.org/10.1071/bt02110

- Jang, J.-S.R., 1993. ANFIS: adaptive-network-based fuzzy inference system. IEEE Trans. Syst. Man Cybern. 23, 665–685. https://doi.org/10.1109/21.256541
- Jiang, D., Dong, C., Ma, Z., Wang, X., Lin, K., Yang, F., Chen, X., 2024. Monitoring saltwater intrusion to estuaries based on UAV and satellite imagery with machine learning models. Remote Sens. Environ. 308, 114198. https://doi.org/10.1016/j.rse.2024.114198
- Jualaong, S., Songnui, A., Thongprajukaew, K., Ninwat, S., Khwanmaung, S., Hahor, W., Khunsaeng, P., Kanghae, H., 2019. Optimal Salinity for Head-Starting Northern River Terrapins (Batagur baska Gray, 1831). Animals 9, 855. https://doi.org/10.3390/ani9110855
- Kao, H.-Y., Lagerloef, G.S.E., Lee, T., Melnichenko, O., Meissner, T., Hacker, P., 2018. Assessment of Aquarius Sea Surface Salinity. Remote Sens. 10, 1341. https://doi.org/10.3390/rs10091341
- Ke, G., Meng, Q., Finley, T., Wang, T., Chen, W., Ma, W., Ye, Q., Liu, T.-Y., 2017. LightGBM: A Highly Efficient Gradient Boosting Decision Tree, in: Advances in Neural Information Processing Systems. Curran Associates, Inc.
- Kelly, M., 2019. The Standard Errors of Persistence. Cent. Econ. Policy Res. https://doi.org/10.2139/ssrn.3398303
- Kerr, Y.H., Waldteufel, P., Wigneron, J.-P., Delwart, S., Cabot, F., Boutin, J.,
  Escorihuela, M.-J., Font, J., Reul, N., Gruhier, C., Juglea, S.E., Drinkwater,
  M.R., Hahne, A., Martín-Neira, M., Mecklenburg, S., 2010. The SMOS
  Mission: New Tool for Monitoring Key Elements of the Global Water Cycle.
  Proc. IEEE 98, 666–687. https://doi.org/10.1109/JPROC.2010.2043032
- Khadim, F.K., Su, H., Xu, L., 2017. A spatially weighted optimization model (SWOM) for salinity mapping in Florida Bay using Landsat images and in situ observations. Phys. Chem. Earth Parts ABC, Physics and Economics of Ecosystem Services Flows 101, 86–101. https://doi.org/10.1016/j.pce.2017.06.001
- Khan, N.M., Rastoskuev, V.V., Sato, Y., Shiozawa, S., 2005. Assessment of hydrosaline land degradation by using a simple approach of remote sensing indicators. Agric. Water Manag., Special Issue on Land and Water Use: Environmental Management Tools and Practices 77, 96–109. https://doi.org/10.1016/j.agwat.2004.09.038
- Khan, N.M., Rastoskuev, V.V., Shalina, E.V., Sato, Y., 2001. Mapping Salt-affected Soils Using Remote Sensing Indicators A Simple Approach With the Use of GIS IDRISI. Presented at the 22nd Asian Conference on Remote Sensing, Singapore.
- Khorram, S., 1985. Development of water quality models applicable throughout the entire San Francisco Bay and Delta. Photogramm. Eng. Remote Sens. 51, 53–62.

- Kuhn, M., Weston, S., Keefer, C., Coulter, N., Quinlan, R., 2023. Cubist: Rule- And Instance-Based Regression Modeling.
- Lagerloef, G., Colomb, F.R., Le Vine, D., Wentz, F., Yueh, S., Ruf, C., Lilly, J., Gunn, J., Chao, Y., Decharon, A., Feldman, G., Swift, C., 2008. The Aquarius/Sac-D Mission: Designed to Meet the Salinity Remote-Sensing Challenge.

  Oceanography 21, 68–81.
- Lavery, P., Pattiaratchi, C., Wyllie, A., Hick, P., 1993. Water quality monitoring in estuarine waters using the Landsat thematic mapper. Remote Sens. Environ. 46, 268–280. https://doi.org/10.1016/0034-4257(93)90047-2
- Li, Z., Zhang, F., Shi, J., Chan, N.W., Tan, M.L., Kung, H., Liu, C., Cheng, C., Cai, Y., Wang, W., Li, X., 2023. Remote sensing for chromophoric dissolved organic matter (CDOM) monitoring research 2003–2022: A bibliometric analysis based on the web of science core database. Mar. Pollut. Bull. 196, 115653. https://doi.org/10.1016/j.marpolbul.2023.115653
- Lintern, A., Webb, J. a., Ryu, D., Liu, S., Bende-Michl, U., Waters, D., Leahy, P., Wilson, P., Western, A.W., 2018. Key factors influencing differences in stream water quality across space. Wiley Interdiscip. Rev. Water 5, e1260. https://doi.org/10.1002/wat2.1260
- Liu, T., Dai, J., Zhao, Y., Tian, S., Nie, Z., Ye, C., 2023. Using remote sensing technology to monitor salt lake changes caused by climate change and melting glaciers: insights from Zabuye Salt Lake in Xizang. J. Oceanol. Limnol. 41, 1258–1276. https://doi.org/10.1007/s00343-022-2138-6
- Lu, Y., Chen, Q., Yu, M., Wu, Z., Huang, C., Fu, J., Yu, Z., Yao, J., 2023. Exploring spatial and environmental heterogeneity affecting energy consumption in commercial buildings using machine learning. Sustain. Cities Soc. 95, 104586. https://doi.org/10.1016/j.scs.2023.104586
- Mabula, M.J., Kisanga, D., Pamba, S., 2023. Application of machine learning algorithms and Sentinel-2 satellite for improved bathymetry retrieval in Lake Victoria, Tanzania. Egypt. J. Remote Sens. Space Sci. 26, 619–627. https://doi.org/10.1016/j.ejrs.2023.07.003
- Mahboobi, H., Shakiba, A., Mirbagheri, B., 2023. Improving groundwater nitrate concentration prediction using local ensemble of machine learning models. J. Environ. Manage. 345, 118782. https://doi.org/10.1016/j.jenvman.2023.118782
- Mainali, J., Chang, H., Chun, Y., 2019. A review of spatial statistical approaches to modeling water quality. Prog. Phys. Geogr. Earth Environ. 43, 801–826. https://doi.org/10.1177/0309133319852003
- Malahlela, O.E., 2019. Spatio-temporal assessment of inland surface water quality using remote sensing data in the wake of changing climate, in: IOP Conference Series: Earth and Environmental Science, 6. IOP Publishing, p. 062012. https://doi.org/10.1088/1755-1315/227/6/062012

- Maliki, A.A.A., Chabuk, A., Sultan, M.A., Hashim, B.M., Hussain, H.M., Al-Ansari, N., 2020. Estimation of Total Dissolved Solids in Water Bodies by Spectral Indices Case Study: Shatt al-Arab River. Water. Air. Soil Pollut. 231, 482. https://doi.org/10.1007/s11270-020-04844-z
- Medina-Lopez, E., 2020. Machine Learning and the End of Atmospheric Corrections: A Comparison between High-Resolution Sea Surface Salinity in Coastal Areas from Top and Bottom of Atmosphere Sentinel-2 Imagery. Remote Sens. 12, 2924. https://doi.org/10.3390/rs12182924
- Medina-Lopez, E., Ureña-Fuentes, L., 2019. High-Resolution Sea Surface Temperature and Salinity in Coastal Areas Worldwide from Raw Satellite Data. Remote Sens. 11, 2191. https://doi.org/10.3390/rs11192191
- Mejía Ávila, D., Torres-Bejarano, F., Martínez Lara, Z., 2022. Spectral indices for estimating total dissolved solids in freshwater wetlands using semi-empirical models. A case study of Guartinaja and Momil wetlands. Int. J. Remote Sens. 43, 2156–2184. https://doi.org/10.1080/01431161.2022.2057205
- Menze, B.H., Kelm, B.M., Masuch, R., Himmelreich, U., Bachert, P., Petrich, W., Hamprecht, F.A., 2009. A comparison of random forest and its Gini importance with standard chemometric methods for the feature selection and classification of spectral data. BMC Bioinformatics 10, 213. https://doi.org/10.1186/1471-2105-10-213
- Metulini, R., Patuelli, R., Griffith, D.A., 2018. A Spatial-Filtering Zero-Inflated Approach to the Estimation of the Gravity Model of Trade. Econometrics 6, 9. https://doi.org/10.3390/econometrics6010009
- Minor, E.C., Pothen, J., Dalzell, B.J., Abdulla, H., Mopper, K., 2006. Effects of salinity changes on the photodegradation and ultraviolet—visible absorbance of terrestrial dissolved organic matter. Limnol. Oceanogr. 51, 2181–2186. https://doi.org/10.4319/lo.2006.51.5.2181
- Mishra, D.R., Ogashawara, I., Gitelson, A.A., 2017. Bio-optical Modeling and Remote Sensing of Inland Waters. Elsevier.
- Montalvo, L.G., 2010. Spectral analysis of suspended material in coastal waters: A comparison between band math equations. Dep. Geol. Univ. P. R. Mayaguez PR USA 1–6.
- Moradi-Majd, N., Fallah-Ghalhari, G., Chatrenor, M., 2022. Estimation of greenhouse gas emission flux from agricultural lands of Khuzestan province in Iran. Environ. Monit. Assess. 194, 811. https://doi.org/10.1007/s10661-022-10497-8
- Moran, P.A.P., 1950. Notes on Continuous Stochastic Phenomena. Biometrika 37, 17–23. https://doi.org/10.2307/2332142
- Morley, S.K., Brito, T.V., Welling, D.T., 2018. Measures of Model Performance Based On the Log Accuracy Ratio. Space Weather 16, 69–88. https://doi.org/10.1002/2017SW001669

- Mushtaq, F., Nee Lala, M.G., 2017. Remote estimation of water quality parameters of Himalayan lake (Kashmir) using Landsat 8 OLI imagery. Geocarto Int. 32, 274–285. https://doi.org/10.1080/10106049.2016.1140818
- Nahvi, A., Daghighi, A., Nazif, S., 2018. The environmental impact assessment of drainage systems: a case study of the Karun river sugarcane development project. Arch. Agron. Soil Sci. 64, 185–195. https://doi.org/10.1080/03650340.2017.1340641
- Nazeer, M., Bilal, M., 2018. Evaluation of Ordinary Least Square (OLS) and Geographically Weighted Regression (GWR) for Water Quality Monitoring: A Case Study for the Estimation of Salinity. J. Ocean Univ. China 17, 305–310. https://doi.org/10.1007/s11802-018-3380-6
- Nguyen, P.T.B., Koedsin, W., McNeil, D., Van, T.P.D., 2018. Remote sensing techniques to predict salinity intrusion: application for a data-poor area of the coastal Mekong Delta, Vietnam. Int. J. Remote Sens. 39, 6676–6691. https://doi.org/10.1080/01431161.2018.1466071
- Nossent, J., Elsen, P., Bauwens, W., 2011. Sobol' sensitivity analysis of a complex environmental model. Environ. Model. Softw. 26, 1515–1525. https://doi.org/10.1016/j.envsoft.2011.08.010
- Nouraki, A., Alavi, M., Golabi, M., Albaji, M., 2021. Prediction of water quality parameters using machine learning models: a case study of the Karun River, Iran. Environ. Sci. Pollut. Res. 28, 57060–57072. https://doi.org/10.1007/s11356-021-14560-8
- Oshan, T.M., Li, Z., Kang, W., Wolf, L.J., Fotheringham, A.S., 2019. mgwr: A Python Implementation of Multiscale Geographically Weighted Regression for Investigating Process Spatial Heterogeneity and Scale. ISPRS Int. J. Geo-Inf. 8, 269. https://doi.org/10.3390/ijgi8060269
- Pahlevan, N., Smith, B., Alikas, K., Anstee, J., Barbosa, C., Binding, C., Bresciani, M., Cremella, B., Giardino, C., Gurlin, D., Fernandez, V., Jamet, C., Kangro, K., Lehmann, M.K., Loisel, H., Matsushita, B., Hà, N., Olmanson, L., Potvin, G., Simis, S.G.H., VanderWoude, A., Vantrepotte, V., Ruiz-Verdù, A., 2022. Simultaneous retrieval of selected optical water quality indicators from Landsat-8, Sentinel-2, and Sentinel-3. Remote Sens. Environ. 270, 112860. https://doi.org/10.1016/j.rse.2021.112860
- Paoletti, M.E., Haut, J.M., Plaza, J., Plaza, A., 2019. Deep learning classifiers for hyperspectral imaging: A review. ISPRS J. Photogramm. Remote Sens. 158, 279–317. https://doi.org/10.1016/j.isprsjprs.2019.09.006
- Peralta, N.R., Assefa, Y., Du, J., Barden, C.J., Ciampitti, I.A., 2016. Mid-Season High-Resolution Satellite Imagery for Forecasting Site-Specific Corn Yield. Remote Sens. 8, 848. https://doi.org/10.3390/rs8100848
- Priyadarshini, R., Sudhakara, B., Sowmya Kamath, S., Bhattacharjee, S., Pruthviraj, U., Gangadharan, K.V., 2023. Water Salinity Assessment Using Remotely Sensed

- Images—A Comprehensive Survey, in: Computer Vision and Machine Intelligence, Lecture Notes in Networks and Systems. Springer Nature, Singapore, pp. 577–589. https://doi.org/10.1007/978-981-19-7867-8 46
- Quinlan, J.R., 1992. Learning with continuous classes, in: 5th Australian Joint Conference on Artificial Intelligence. Presented at the 5th Australian joint conference on artificial intelligence, pp. 343–348.
- Rey, S.J., Anselin, L., 2010. PySAL: A Python Library of Spatial Analytical Methods, in: Fischer, M.M., Getis, A. (Eds.), Handbook of Applied Spatial Analysis: Software Tools, Methods and Applications. Springer, Berlin, Heidelberg, pp. 175–193. https://doi.org/10.1007/978-3-642-03647-7 11
- Röttgers, R., McKee, D., Utschig, C., 2014. Temperature and salinity correction coefficients for light absorption by water in the visible to infrared spectral region. Opt. Express 22, 25093–25108. https://doi.org/10.1364/OE.22.025093
- Rouse, J.W., Haas, R.H., Schell, J.A., Deering, D.W., 1974. Monitoring vegetation systems in the Great Plains with ERTS. NASA Spec. Publ. 351, 309–317.
- Rusydi, A.F., 2018. Correlation between conductivity and total dissolved solid in various type of water: A review, in: IOP Conference Series: Earth and Environmental Science. IOP publishing, p. 012019. https://doi.org/10.1088/1755-1315/118/1/012019
- Schemel, L.E., 2001. Simplified conversions between specific conductance and salinity units for use with data from monitoring stations. Interag. Ecol. Program Newsl. 14, 17–18.
- Seabold, S., Perktold, J., 2010. Statsmodels: Econometric and Statistical Modeling with Python, in: The 9th Python in Science Conference. Austin, Texas, pp. 92–96.
- Sebilian Wittyngham, S., Moderan, J., Boyer, K.E., 2019. Temperature and salinity effects on submerged aquatic vegetation traits and susceptibility to grazing. Aquat. Bot. 158, 103119. https://doi.org/10.1016/j.aquabot.2019.05.004
- Servén, D., Brummitt, C., Abedi, H., Hlink, 2018. pyGAM: Generalized Additive Models in Python. Zenodo. https://doi.org/10.5281/zenodo.1208723
- Shahin, M.A., Maier, H.R., Jaksa, M.B., 2004. Data Division for Developing Neural Networks Applied to Geotechnical Engineering. J. Comput. Civ. Eng. 18, 105–114. https://doi.org/10.1061/(ASCE)0887-3801(2004)18:2(105)
- Shahraki, M.Z., Keivany, Y., Dorche, E.E., Blocksom, K., Bruder, A., Flotemersch, J., Bănăduc, D., 2023. Distribution and Expansion of Alien Fish Species in the Karun River Basin, Iran. Fishes 8, 538. https://doi.org/10.3390/fishes8110538
- Siddorn, J.R., Bowers, D.G., Hoguane, A.M., 2001. Detecting the Zambezi River Plume using Observed Optical Properties. Mar. Pollut. Bull. 42, 942–950. https://doi.org/10.1016/S0025-326X(01)00053-4

- Smith, B., Pahlevan, N., Schalles, J., Ruberg, S., Errera, R., Ma, R., Giardino, C.,
  Bresciani, M., Barbosa, C., Moore, T., Fernandez, V., Alikas, K., Kangro, K.,
  2021. A Chlorophyll-a Algorithm for Landsat-8 Based on Mixture Density
  Networks. Front. Remote Sens. 1.
- Smola, A.J., Schölkopf, B., 2004. A tutorial on support vector regression. Stat. Comput. 14, 199–222. https://doi.org/10.1023/B:STCO.0000035301.49549.88
- Sobol', I.M., 1993. Sensitivity Estimates for Non-linear Mathematical Models. Math Model Comput Exp 1, 407–414.
- Sotomayor, L.N., Cracknell, M.J., Musk, R., 2023. Supervised machine learning for predicting and interpreting dynamic drivers of plantation forest productivity in northern Tasmania, Australia. Comput. Electron. Agric. 209, 107804. https://doi.org/10.1016/j.compag.2023.107804
- Sumner, D.M., Belaineh, G., 2005. Evaporation, precipitation, and associated salinity changes at a humid, subtropical estuary. Estuaries 28, 844–855. https://doi.org/10.1007/BF02696014
- Tessema, N., Yadeta, D., Kebede, A., Ayele, G.T., 2022. Soil and Irrigation Water Salinity, and Its Consequences for Agriculture in Ethiopia: A Systematic Review. Agriculture 13, 109. https://doi.org/10.3390/agriculture13010109
- Tobler, W.R., 1970. A Computer Movie Simulating Urban Growth in the Detroit Region. Econ. Geogr. 46, 234–240. https://doi.org/10.2307/143141
- Topp, S.N., Pavelsky, T.M., Jensen, D., Simard, M., Ross, M.R.V., 2020. Research Trends in the Use of Remote Sensing for Inland Water Quality Science: Moving Towards Multidisciplinary Applications. Water 12, 169. https://doi.org/10.3390/w12010169
- Uncles, R.J., Stephens, J.A., 2011. The Effects of Wind, Runoff and Tides on Salinity in a Strongly Tidal Sub-estuary. Estuaries Coasts 34, 758–774. https://doi.org/10.1007/s12237-010-9365-3
- Urquhart, E.A., Zaitchik, B.F., Hoffman, M.J., Guikema, S.D., Geiger, E.F., 2012. Remotely sensed estimates of surface salinity in the Chesapeake Bay: A statistical approach. Remote Sens. Environ. 123, 522–531. https://doi.org/10.1016/j.rse.2012.04.008
- U.S. Geological Survey, 2019. Specific conductance: U.S. Geological Survey Techniques and Methods, Techniques and Methods. Reston, VA, book 9, chap. A6.3, 15 p. https://doi.org/10.3133/tm9A6.3
- Vandermeulen, R.A., Arnone, R., Ladner, S., Martinolich, P., 2014. Estimating sea surface salinity in coastal waters of the Gulf of Mexico using visible channels on SNPP-VIIRS, in: Ocean Sensing and Monitoring VI. Presented at the Ocean Sensing and Monitoring VI, SPIE, pp. 56–62. https://doi.org/10.1117/12.2053417

- Verrelst, J., Rivera, J.P., 2017. Chapter 16 A Global Sensitivity Analysis Toolbox to Quantify Drivers of Vegetation Radiative Transfer Models, in: Petropoulos, G.P., Srivastava, P.K. (Eds.), Sensitivity Analysis in Earth Observation Modelling. Elsevier, pp. 319–339. https://doi.org/10.1016/B978-0-12-803011-0.00016-1
- Vovk, V., 2013. Kernel Ridge Regression, in: Schölkopf, B., Luo, Z., Vovk, V. (Eds.), Empirical Inference: Festschrift in Honor of Vladimir N. Vapnik. Springer, Berlin, Heidelberg, pp. 105–116. https://doi.org/10.1007/978-3-642-41136-6\_11
- Vuille, M., Baumgartner, M.F., 1993. Hydrologic investigations in the north Chilean Altiplano using Landsat MSS and TM data. Geocarto Int. 8, 35–45. https://doi.org/10.1080/10106049309354418
- Wagner, R.J., Jr, R.W.B., Oblinger, C.J., Smith, B.A., 2006. Guidelines and standard procedures for continuous water-quality monitors: Station operation, record computation, and data reporting. Tech. Methods. https://doi.org/10.3133/tm1D3
- Wang, F., Xu, Y.J., 2008. Development and application of a remote sensing-based salinity prediction model for a large estuarine lake in the US Gulf of Mexico coast. J. Hydrol. 360, 184–194. https://doi.org/10.1016/j.jhydrol.2008.07.036
- Warner, J., Sexauer, J., scikit-fuzzy, twmeggs, alexsavio, Unnikrishnan, A., Castelão, G., Pontes, F.A., Uelwer, T., pd2f, laurazh, Batista, F., alexbuy, Broeck, W.V. den, Song, W., Badger, T.G., Pérez, R.A.M., Power, J.F., Mishra, H., Trullols, G.O., Hörteborn, A., 99991, 2019. JDWarner/scikit-fuzzy: Scikit-Fuzzy version 0.4.2. https://doi.org/10.5281/zenodo.3541386
- Werdell, P.J., Franz, B.A., Lefler, J.T., Robinson, W.D., Boss, E., 2013. Retrieving marine inherent optical properties from satellites using temperature and salinity-dependent backscattering by seawater. Opt. Express 21, 32611–32622. https://doi.org/10.1364/OE.21.032611
- Williams, C., Rasmussen, C., 1995. Gaussian Processes for Regression, in: Advances in Neural Information Processing Systems. MIT Press.
- Xie, Z., Zhang, C., Berry, L., 2013. Geographically weighted modelling of surface salinity in Florida Bay using Landsat TM data. Remote Sens. Lett. 4, 75–83. https://doi.org/10.1080/2150704X.2012.693218
- Zhang, C., Xie, Z., Roberts, C., Berry, L., Chen, G., 2012. Salinity Assessment in Northeast Florida Bay Using Landsat TM Data. Southeast. Geogr. 52, 267–281.
- Zhang, X., Hu, L., 2021. Light Scattering by Pure Water and Seawater: Recent Development. J. Remote Sens. 2021. https://doi.org/10.34133/2021/9753625
- Zhang, X., Hu, L., He, M.-X., 2009. Scattering by pure seawater: Effect of salinity. Opt. Express 17, 5698–5710. https://doi.org/10.1364/OE.17.005698
- Zhao, J., Temimi, M., Ghedira, H., 2017. Remotely sensed sea surface salinity in the hyper-saline Arabian Gulf: Application to Landsat 8 OLI data. Estuar. Coast. Shelf Sci. 187, 168–177. https://doi.org/10.1016/j.ecss.2017.01.008

**Table 1.** Summary of studies that have used moderate spatial-resolution sensors to map salinity, in chronological order. NIR: near-infrared band, SWIR: shortwave infrared band, MSS: Landsat Multispectral Scanner, TM: Landsat Thematic Mapper, OLI: Landsat Operational Line Imager, ETM+: Landsat Enhanced Thematic Mapper Plus, and MSI: Sentinel-2 MSI.

Sensor(s)	Band(s) and Feature(s)	Empirical Model(s)	Reference
MSS	Red and NIR 1	LR	(Khorram, 1985)
TM	NIR and SWIR 2	LR	(Lavery et al., 1993)
MSS and TM	Blue, NIR, and SWIR 2	LR	(Vuille and Baumgartner, 1993)
TM	Blue, Green, Red, NIR, and SWIR 1	LR and ridge regression	(Wang and Xu, 2008)
TM	Blue, Red, and NIR	LR	(Zhang et al., 2012)

TM	First three principal component analysis components	GWR	(Xie et al., 2013)
TM	Blue, Green, Red, NIR, SWIR 1, and SWIR 2	SWOM	(Khadim et al., 2017)
OLI	Coastal Aerosol, Blue, Green, and Red	LR	(Zhao et al., 2017)
OLI	Red	Non-linear Regression	(Mushtaq and Nee Lala, 2017)
TM	Blue, Red, and NIR	LR and GWR	(Nazeer and Bilal, 2018)
OLI	Blue, Green, Red, and SWIR 2	MLR, DT, and RF	(Nguyen et al., 2018)
ASTER	Red, SWIR 2, and SWIR 4	LR	(Abdelmalik, 2018)
OLI	Coastal Aerosol, Blue, and Green	SVR	(Ansari and Akhoondzadeh, 2019)
MSI	All Sentinel-2 bands and image properties	ANN	(Medina-Lopez and Ureña- Fuentes, 2019)
OLI	Blue, Green, and Red	LR	(Ferdous et al., 2019)
OLI	Salinity index 2	LR	(Maliki et al., 2020)
OLI	Coastal Aerosol, Blue, and Green	LR, SVR, and MLP	(Ansari and Akhoondzadeh, 2020)
TM and OLI	Blue, Green, and Red	MLR	(Ferdous and Rahman, 2020)
MSI	All Sentinel-2 bands and image properties	ANN	(Medina-Lopez, 2020)
OLI	Coastal Aerosol, Blue, and Green	MLP and SVR	(Ansari and Akhoondzadeh, 2021)

OLI and MSI	Blue, Green, and Red	ANN, MLR, and ANFIS	(Bayati and Danesh-Yazdi, 2021)
MSI	Red edge 2, Red edge 3, NIR 1, NIR 2, SWIR 2, and SWIR 1	LR, RF and AdaBoost	(Borovskaya et al., 2022)
OLI	Salinity index 5	LR	(Adjovu et al., 2022)
TM and OLI	Blue, NIR, and SWIR 2	LR	(Chatterjee and Bhadra, 2023)
ETM+ and OLI	Blue, Green, Red, NIR, SWIR 1, and SWIR 2	LightGBM, RF, and ANN	(Dai et al., 2023)
MSI	All Sentinel-2 bands except from SWIR 3 and SWIR 4	DT, RF, XGBoost, AdaBoost	(Jiang et al., 2024)

Table 2. Indices were used in this study.  $\rho$  represents the surface reflectance.

indices	Formula	Reference	
Salinity index 1	$\sqrt{ ho_{Blue}  imes  ho_{Red}}$	(Khan et al., 2001)	
Salinity index 2	$\sqrt{ ho_{Blue}  imes  ho_{Green}}$	(Maliki et al., 2020)	
Salinity index 3	$\sqrt{ ho_{Green}^2 +  ho_{Red}^2}$	(Douaoui et al., 2006)	
Salinity index 4	$\sqrt{\rho_{Green}^2 + \rho_{Red}^2 + \rho_{NIR}^2}$	(Douaoui et al., 2006)	
Salinity index 5	$ ho_{Red}  imes  ho_{Green}$	(Maliki et al., 2020)	

Salinity index 6	$\sqrt{ ho_{Green}^2  imes  ho_{NIR}^2}$	(Bouaziz et al., 2011)
Salinity index 7	PBlue/PGreen	(Ferdous and Rahman, 2020)
NDSI	$( ho_{Red}- ho_{NIR})/( ho_{Red}+ ho_{NIR})$	(Khan et al., 2005)
NSMI	$(\rho_{Red} + \rho_{Green} - \rho_{Blue})/(\rho_{Red} + \rho_{Green} + \rho_{Blue})$	(Montalvo, 2010)
NDSSI	$( ho_{Blue}- ho_{NIR})/( ho_{Blue}+ ho_{NIR})$	(Hossain et al., 2010)
BR	$ ho_{Green}/ ho_{Blue}$	(Montalvo, 2010)
EGRI	$ ho_{Green}/( ho_{Blue}+ ho_{CoastalAerosol})$	(Malahlela, 2019)
NDVI	$( ho_{NIR}- ho_{Red})/( ho_{NIR}+ ho_{Red})$	(Rouse et al., 1974)
WSRI	$1-[( ho_{SWRI1}- ho_{Blue})/ ho_{Red}]$	(Malahlela, 2019)

**Table 3.** Date of satellite image acquisition and *in situ* data collection. Matchups for each date are available at the stations listed in the Station(s) column. For other stations, either field data were not collected, or the data were masked due to cloud cover.

Date of satellite image acquisition	Date of <i>in situ</i> data collection	Station(s)
19 June 2013	19 June 2013	Gotvand, Shushtar, Shoteyt, Gargar, Dez, Ahvaz
26 June 2013	25 June 2013	Alikale
12 July 2013	14 July 2013	Alikale
13 August 2013	13 August 2013	Alikale
22 August 2013	24 August 2013	Gotvand, Shushtar, Shoteyt, Gargar, Dez, Ahvaz, Abadan
23 September 2013	25 September 2013	Gotvand, Shushtar, Shoteyt, Gargar, Dez, Ahvaz, Abadan
25 October 2013	26 October 2013	Gotvand
28 December 2013	29 December 2013	Gotvand, Shushtar, Shoteyt, Gargar, Dez, Ahvaz, Abadan
02 March 2014	01 March 2014	Gotvand, Shushtar, Shoteyt, Gargar, Dez, Ahvaz, Abadan
03 April 2014	05 April 2014	Gotvand, Shushtar, Shoteyt, Gargar, Dez, Ahvaz, Abadan
26 April 2014	28 April 2014	Alikale
10 September 2014	08 September 2014	Gotvand, Shushtar, Shoteyt, Gargar, Dez, Ahvaz, Abadan
03 October 2014	04 October 2014	Alikale

15 December 2014	14 December 2014	Gotvand, Shushtar, Shoteyt, Gargar, Dez, Ahvaz, Abadan
01 February 2015	01 February 2015	Gotvand, Shushtar, Shoteyt, Gargar, Dez, Ahvaz, Abadan
18 July 2015	16 July 2015	Alikale
04 September 2015	03 September 2015	Alikale
24 April 2016	26 April 2016	Gotvand, Shushtar, Shoteyt, Gargar, Dez, Ahvaz
29 July 2016	28 July 2016	Gotvand, Shushtar, Shoteyt, Gargar, Dez, Ahvaz, Abadan
01 October 2016	29 September 2016	Gotvand, Shushtar, Shoteyt, Gargar, Dez, Ahvaz
21 January 2017	23 January 2017	Abadan
13 May 2017	14 May 2017	Gotvand, Shushtar, Shoteyt, Gargar, Dez, Ahvaz, Abadan
07 December 2017	05 December 2017	Gotvand, Gargar, Ahvaz, Abadan
10 July 2018	12 July 2018	Alikale

**Table 4.** Minimum, maximum, and average salinity values (psu) and number of observations (N) at the eight salinity measurement stations.

Station	Min.	Ave.	Max.	N
Alikale	0.19	0.22	0.28	8
Gotvand	0.38	0.57	0.76	15
Shushtar	0.42	0.66	0.85	13
Shoteyt	0.65	0.85	1.00	13
Gargar	1.13	1.56	1.93	14
Dez	0.36	1.11	1.64	13
Ahvaz	0.89	1.11	1.51	14
Abadan	1.28	1.50	1.90	12

 Table 5. Results of feature engineering.

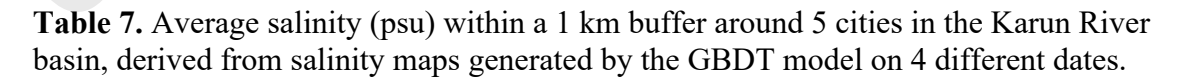
No.	Feature	$S_T$	S <sub>T</sub>	RFFIS	RFFIS Rank	Correlation	Correlation Rank	Mean Rank
1	Red	2.77E- 01	1	9.20E- 02	3	1.79E-01	4	2.7
2	Salinity index 3	2.66E- 01	2	6.33E- 02	6	1.82E-01	2	3.3
3	Salinity index 4	1.86E- 01	3	7.13E- 02	4	1.43E-01	5	4.0
4	NSMI	1.85E- 03	10	1.38E- 01	1	2.36E-01	1	4.0
5	Salinity index 6	8.82E- 02	5	4.59E- 02	8	1.17E-01	7	6.7
6	Salinity index 2	1.93E- 03	9	5.17E- 02	7	8.85E-02	9	8.3
7	Green	3.79E- 03	8	3.17E- 02	14	1.80E-01	3	8.3

8	Salinity index 5	2.64E- 04	15	1.20E- 01	2	8.24E-02	10	9.0
9	EGRI	7.13E- 04	12	6.75E- 02	5	3.15E-02	14	10.3
10	Salinity index 7	1.31E- 01	4	9.98E- 03	21	1.37E-01	6	10.3
11	Salinity index 1	1.53E- 02	7	2.23E- 02	17	1.07E-01	8	10.7
12	Blue	2.44E- 02	6	1.30E- 02	19	3.38E-02	13	12.7
13	SWIR 1	4.26E- 04	14	3.83E- 02	11	5.89E-03	18	14.3
14	SWIR 2	1.86E- 04	16	4.31E- 02	9	2.67E-03	20	15.0
15	NDVI	1.20E- 05	19	3.09E- 02	15	3.71E-02	11	15.0
16	BR	6.60E- 04	13	3.23E- 02	12	1.28E-03	21	15.3
17	NDSSI	1.35E- 04	17	4.01E- 02	10	3.50E-03	19	15.3
18	NDSI	1.20E- 05	19	2.52E- 02	16	3.71E-02	11	15.3
19	WSRI	1.03E- 04	18	3.17E- 02	13	2.40E-02	16	15.7
20	Coastal Aerosol	7.36E- 04	11	1.24E- 02	20	1.66E-02	17	16.0
21	NIR	1.00E- 06	21	1.91E- 02	18	2.94E-02	15	18.0

**Table 6.** Number of observations (N) and RMSE for each station between measured and estimated salinity using GBDT trained on all dataset (N = 102).

Station	RMSE (psu)	N
Alikale	0.10	8
Gotvand	0.08	15
Shushtar	0.10	13
Shoteyt	0.13	13
Gargar	0.11	14
Dez	0.11	13
Ahvaz	0.06	14

Abadan	0.19	12
--------	------	----



Dete	City						
Date	Gotvand	Shushtar	Ahvaz	Khorramshahr	Abadan		

19 June 2013	0.58	0.79	1.07	1.05	0.72
01 February 2015	0.47	0.51	1.08	0.69	0.97
05 September 2018	0.56	0.54	1.06	0.61	0.96
11 May 2022	0.79	0.91	1.06	1.13	0.93

- **Fig. 1.** Study area (Karun River, Khuzestan, Iran). Overview of 8 salinity sampling stations (red) along the Karun River. Google Earth Pro and Landsat 8 OLI images of each station are shown on the right side of the map. The yellow line on each image indicates the river's width at the respective station.
- Fig. 2. Correlation of features with salinity measurements and within each other.
- **Fig. 3**. R<sup>2</sup> values for each model using different feature combinations. The #Feature refers to the feature number in Table 5, indicating that the feature with this number, along with those with lower numbers, yields the highest R<sup>2</sup>, as shown in the top-left corner of each panel
- **Fig. 4.** Scatter plot illustrating the relationship between measured and estimated salinity using test data (N=30). Each point represents a model prediction, with the name and class of each model displayed at the bottom right corner. The top right and left corners display the statistical metrics:  $R^2$ , RMSE, RMSLE, β, and ε. Asterisks denote Pearson correlations: \* p < 0.05, \*\* p < 0.01, \*\*\* p < 0.001, \*\*\*\* p < 0.0001. The bottom left corner shows the number of selected features in red. A dashed line represents the 1:1 diagonal line for reference, while a solid-colored line depicts the fitted regression line. Contour lines, derived from kernel density estimates, show data distributions.
- Fig. 5. Box plot depicting the distribution of test data (N = 30). Each box displays the median and interquartile range, while the whiskers represent values within 1.5 times the interquartile range from the lower and upper quartiles. White circles indicate outliers beyond this range.
- **Fig. 6.** Scatter plot illustrating standardized local Moran's I, showcasing relationships between observations with high and low values and their respective neighbors: high-high (HH), low-low (LL), high-low (HL), and low-high (LH). Dashed lines mark the origin axes at (0,0), while the solid black line represents the OLS fit line between standardized local Moran's I (dependent variable: y) and the spatial lag of standardized local Moran's I (independent variable: x). The OLS formula is displayed at the bottom. The global Moran's I value, the global Z-Score, and the p-value is shown at the top left. The p-value, indicating significance levels, is denoted by asterisks: \* p < 0.05, \*\* p < 0.01, \*\*\* p < 0.001, \*\*\*\* p < 0.001. Model names are presented at the bottom right.
- **Fig. 7.** Karun River salinity maps generated by the GBDT model using the entire dataset (N=102) on (a) 13 June 2013, (b) 01 February 2015, (c) 05 September 2018, and (d) 11 May 2022. Measured salinity at stations with available data is shown in red, and estimated salinity is shown in blue.

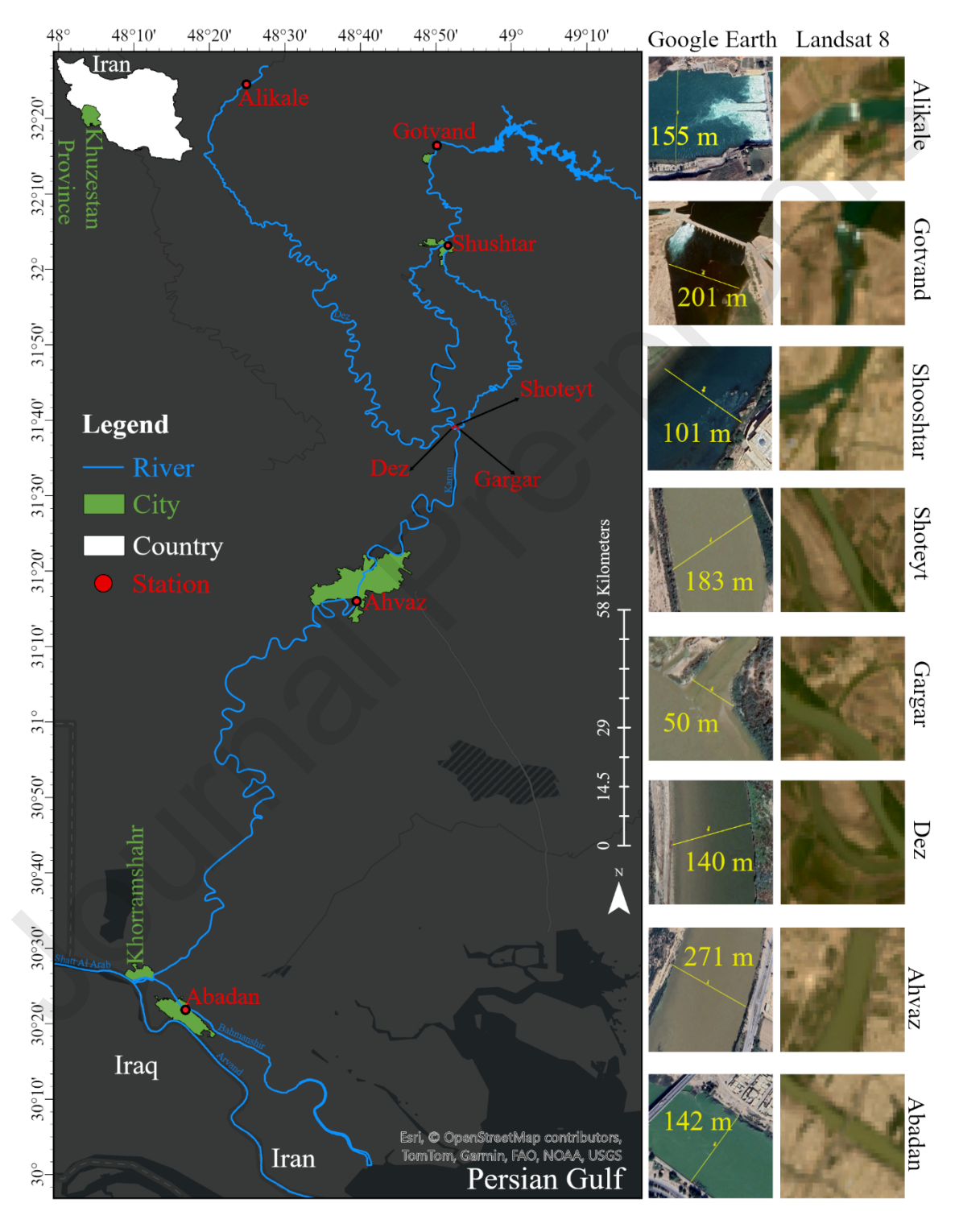


**Fig. 1.** Study area (Karun River, Khuzestan, Iran). Overview of 8 salinity sampling stations (red) along the Karun River. Google Earth Pro and Landsat 8 OLI images of

each station are shown on the right side of the map. The yellow line on each image indicates the river's width at the respective station.

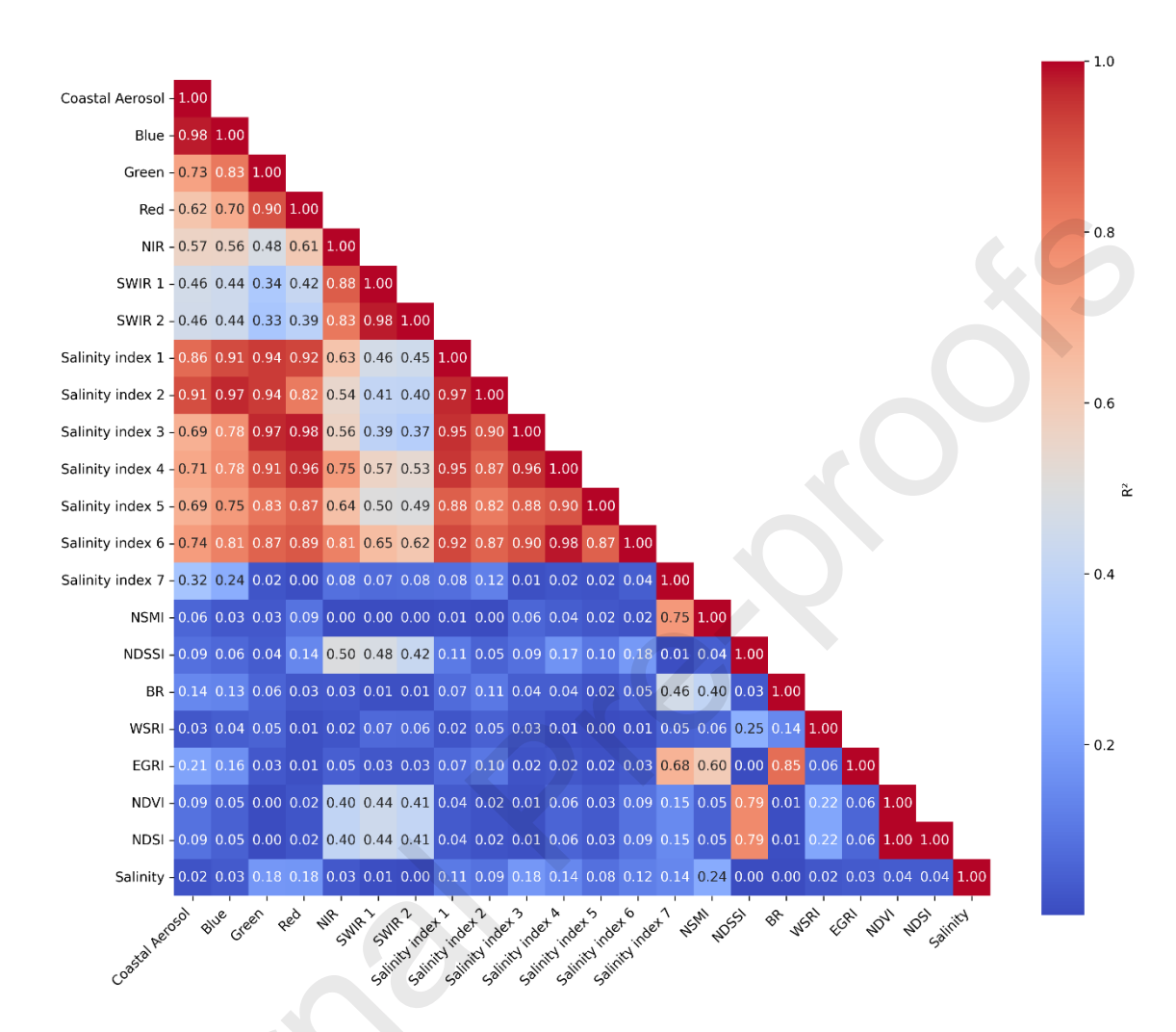
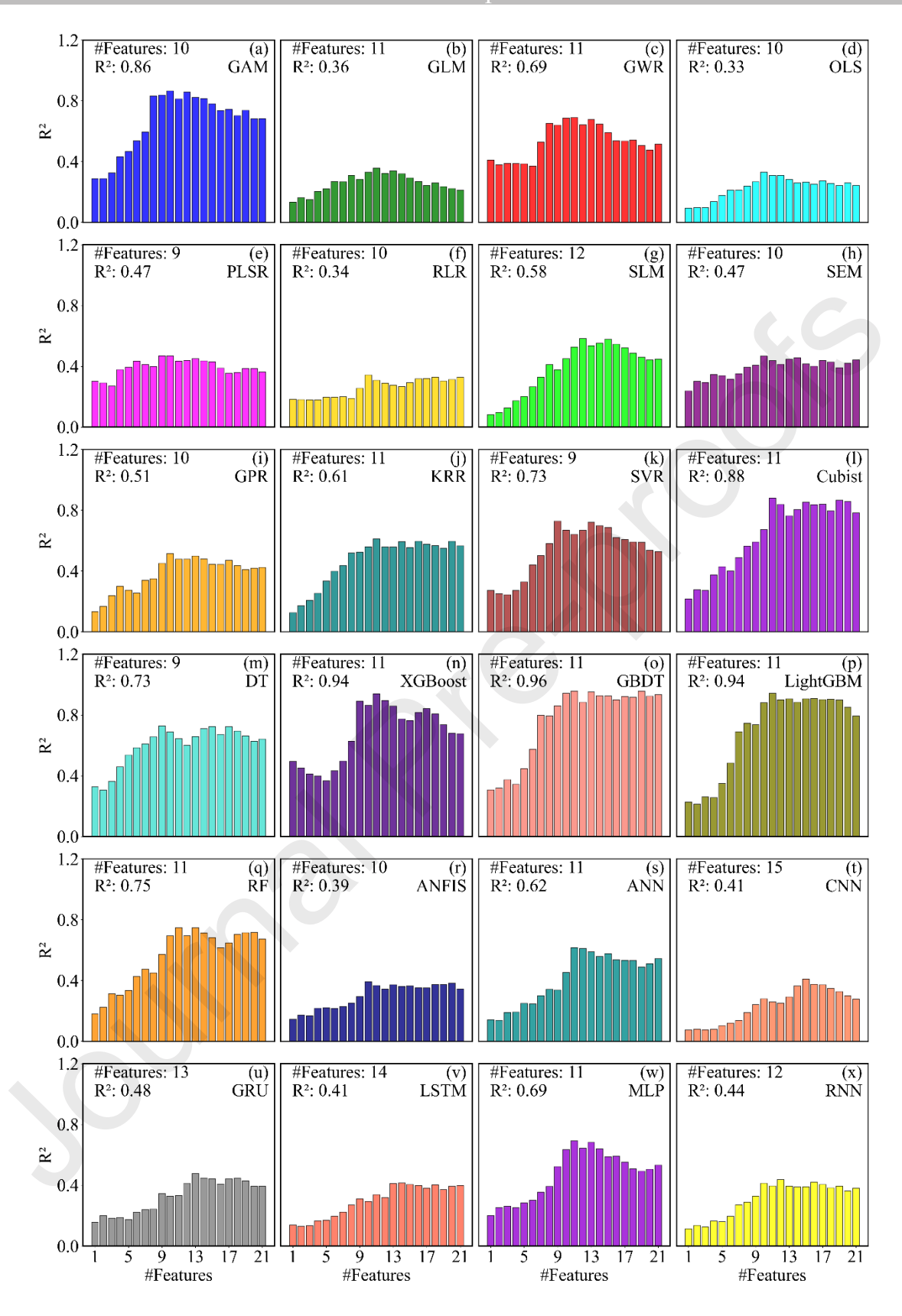
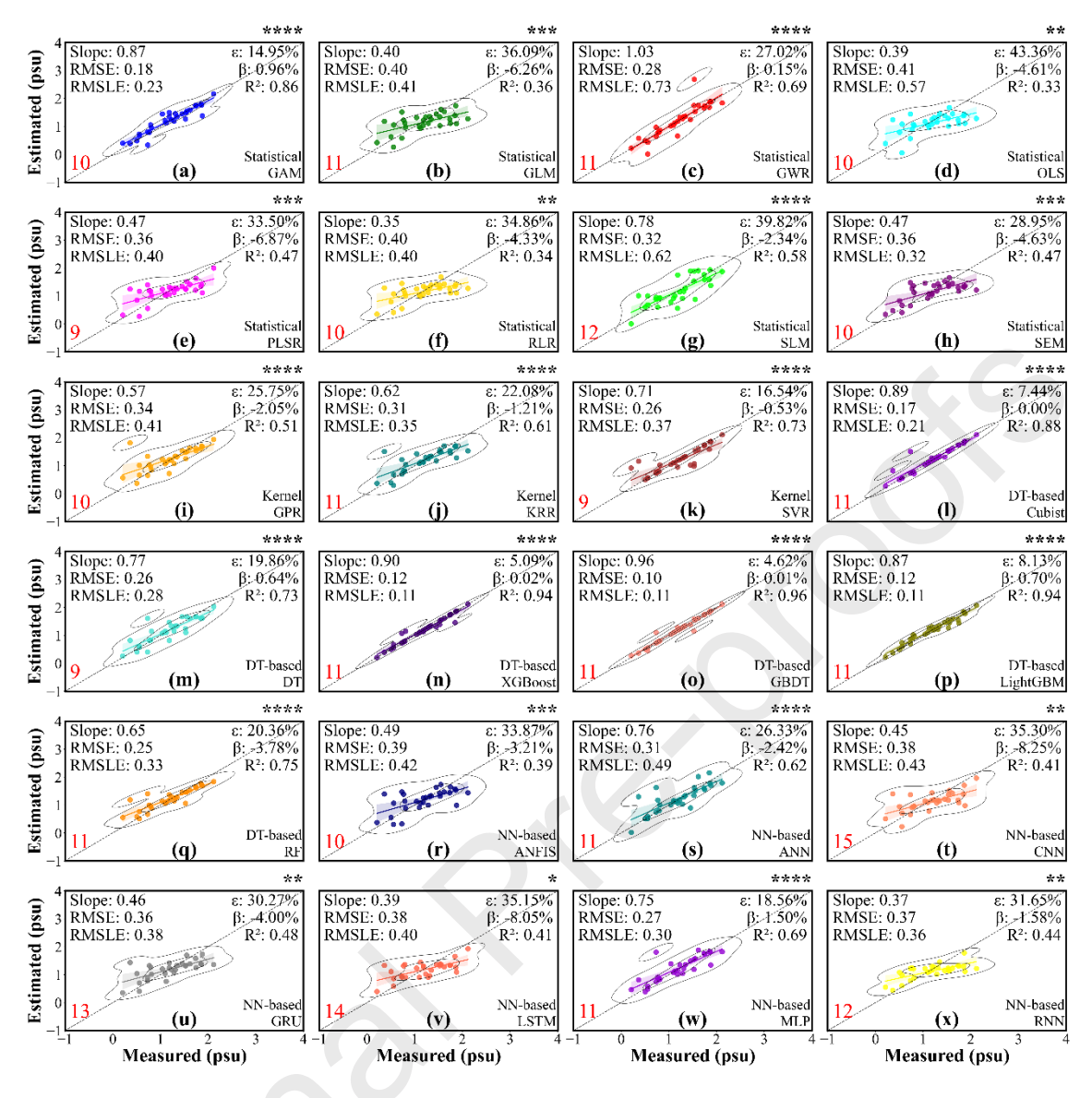


Fig. 2. Correlation of features with salinity measurements and within each other.



**Fig. 3**. R<sup>2</sup> values for each model using different feature combinations. The #Feature refers to the feature number in Table 5, indicating that the feature with this number, along with those with lower numbers, yields the highest R<sup>2</sup>, as shown in the top-left corner of each panel.



**Fig. 4.** Scatter plot illustrating the relationship between measured and estimated salinity using test data (N=30). Each point represents a model prediction, with the name and class of each model displayed at the bottom right corner. The top right and left corners display the statistical metrics:  $R^2$ , RMSE, RMSLE, β, and ε. Asterisks denote Pearson correlations: \* p < 0.05, \*\* p < 0.01, \*\*\*\* p < 0.001, \*\*\*\* p < 0.0001. The bottom left corner shows the number of selected features in red. A dashed line represents the 1:1 diagonal line for reference, while a solid-colored line depicts the fitted regression line. Contour lines, derived from kernel density estimates, show data distributions.

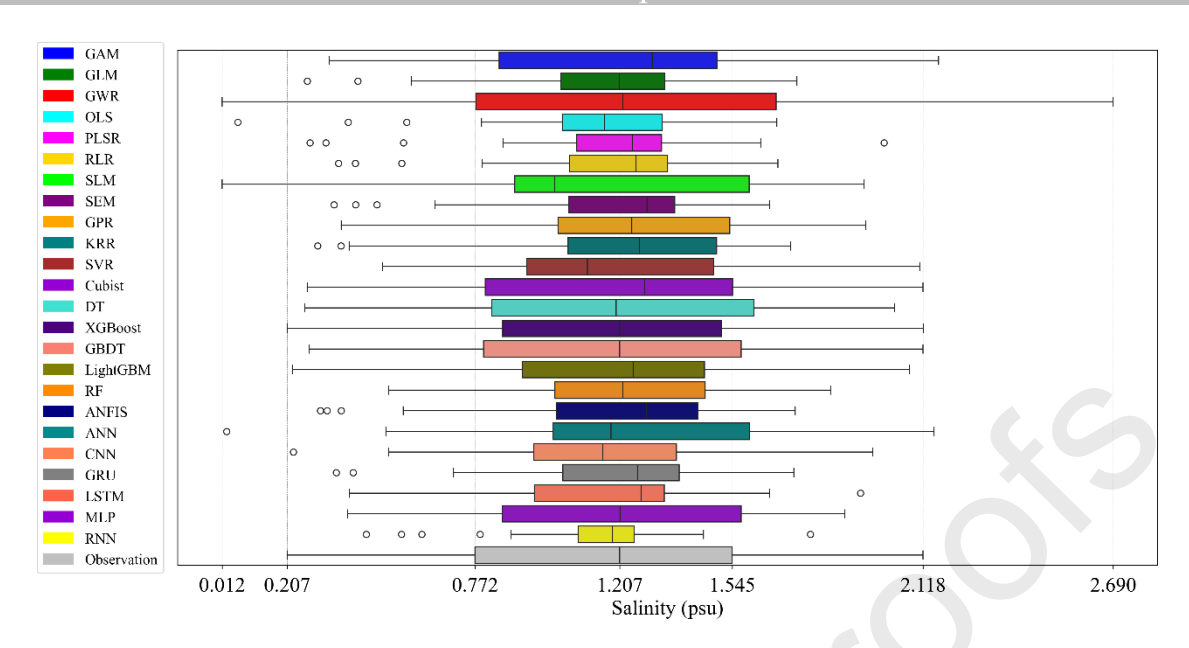
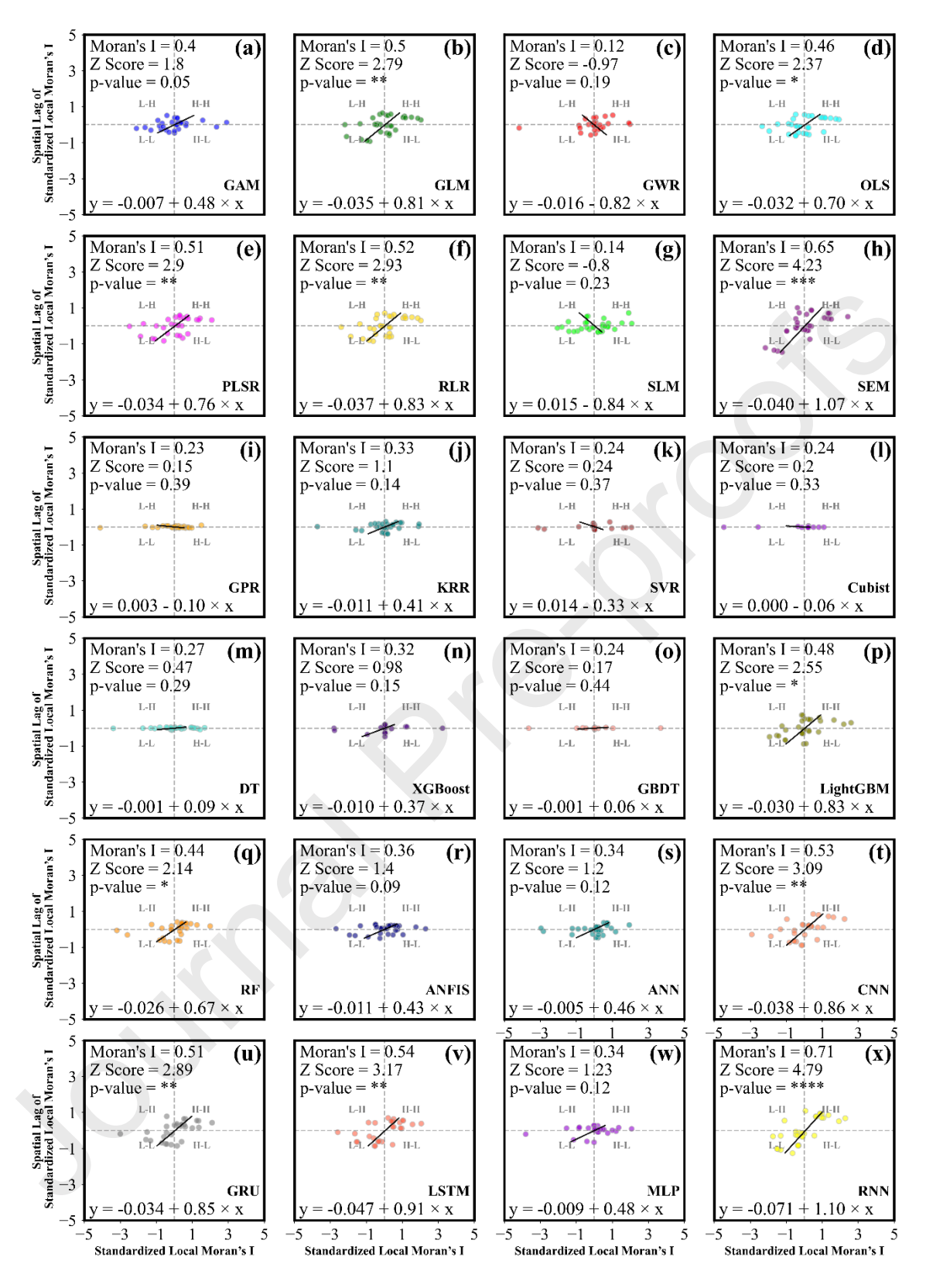
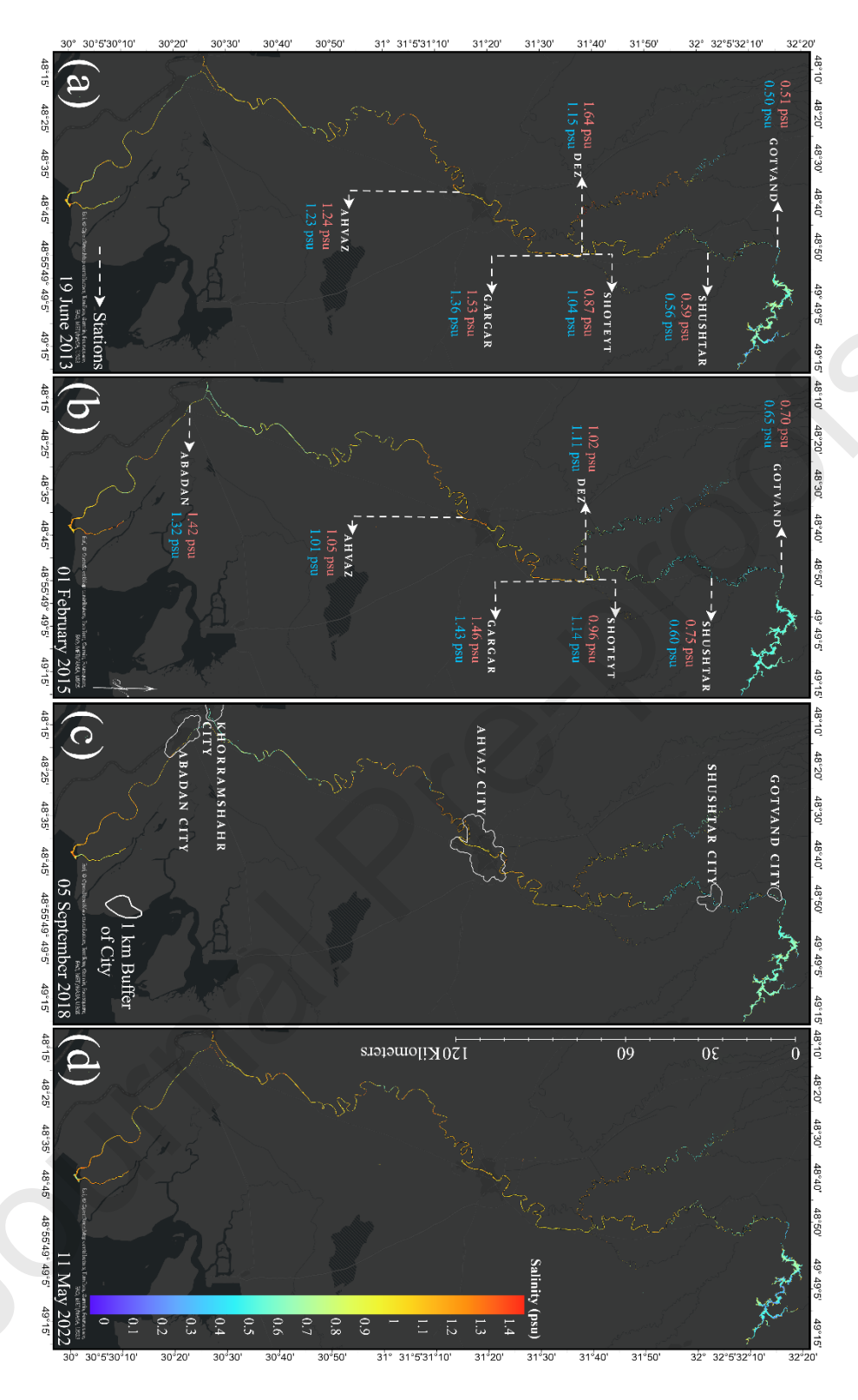


Fig. 5. Box plot depicting the distribution of test data (N = 30). Each box displays the median and interquartile range, while the whiskers represent values within 1.5 times the interquartile range from the lower and upper quartiles. White circles indicate outliers beyond this range.



**Fig. 6.** Scatter plot illustrating standardized local Moran's I, showcasing relationships between observations with high and low values and their respective neighbors: high-high (HH), low-low (LL), high-low (HL), and low-high (LH). Dashed lines mark the origin axes at (0,0), while the solid black line represents the OLS fit line between standardized local Moran's I (dependent variable: y) and the spatial lag of standardized local Moran's I (independent variable: x). The OLS formula is displayed **at** the bottom.

The global Moran's I value, the global Z-Score, and the p-value is shown at the top left. The p-value, indicating significance levels, is denoted by asterisks: \* p < 0.05, \*\* p < 0.01, \*\*\* p < 0.001, \*\*\*\* p < 0.0001. Model names are presented at the bottom right.



**Fig. 7.** Karun River salinity maps generated by the GBDT model using the entire dataset (N=102) on (a) 13 June 2013, (b) 01 February 2015, (c) 05 September 2018, and (d) 11 May 2022. Measured salinity at stations with available data is shown in red, and estimated salinity is shown in blue.

### **Declaration of Competing Interest**

The authors declare that they have no known competing financial interests or personal relationships that could have appeared to influence the work reported in this paper.